J. Fluid Mech. (1996), vol. 310, pp. 293–324

Symmetry-breaking bifurcations in spherical Couette flow

By OLEG Yu. ZIKANOV†

Institute for Problems in Mechanics, Russian Academy of Science,
101 Vernadskii Ave., Moscow 117526, Russia

(Received 11 October 1994 and in revised form 2 November 1995)

The solutions of the nonlinear and linearized Navier–Stokes equations are computed to investigate the instabilities and the secondary two- and three-dimensional regimes in the flow of an incompressible viscous fluid in a thin gap between two concentric differentially rotating spheres. The numerical technique is finite difference in the radial direction, spectral in the azimuthal direction, and pseudo-spectral in the meridional direction. The study follows the experiments by Yavorskaya, Belyaev and co-workers in which a variety of steady axisymmetric and three-dimensional travelling wave secondary regimes was observed in the case of a thin layer and both boundary spheres rotating. In agreement with the experimental results three different types of symmetry-breaking primary bifurcations of the basic equilibrium are detected in the parameter range under consideration.

1. Introduction

The results to be discussed in the present paper concern the behaviour of the flow of an incompressible viscous fluid contained between two concentric spheres rotating about a common axis with fixed angular velocities. This spherical Couette flow (abbreviated frequently as SCF) represents the natural generalization of its simpler analogues such as plane and circular Couette flows and the flow between rotating disks. The flow is of basic interest for understanding global astrophysical and geophysical processes which depend crucially on two factors: rotation and spherical geometry.

An important property of the system under consideration is that it displays two types of symmetry. The fluid equations, boundary conditions and thus the basic flow are reflection-symmetric with respect to the equatorial plane and symmetric with respect to azimuthal translations $\varphi \to \varphi + l(mod 2\pi)$ (rotationally symmetric). These symmetries are responsible for many features of bifurcations of the problem. If the basic flow (or another equatorially symmetric steady flow) loses stability to an equatorially antisymmetric eigenmode, then the bifurcation is necessarily an equatorial symmetry-breaking pitchfork. Furthermore, Ruelle (1973) has pointed out that a bifurcation breaking translational symmetry typically leads to travelling wave solutions. As will be discussed in the present paper, such consequences of symmetry properties manifest themselves in full measure in spherical Couette flow.

† Present address: Institut für Strömungsmechanik, Technische Universität Dresden, 01062 Dresden, Germany.

For brevity, the terms reflection-symmetric and anti-reflection symmetric will always denote symmetry with respect to the equator.

Three dimensionless parameters completely specify the problem – the relative gap size $\delta = (R_2 - R_1)/R_1$, the Reynolds number $Re_1 = R_1\Omega_1/\nu$ and the angular velocity ratio $\omega = \Omega_2/\Omega_1$ or, alternatively, the second Reynolds number $Re_2 = R_2\Omega_2/\nu$, where R_i and Ω_i $(i = 1, 2)$ are the radii and the angular velocities of the boundary spheres, ν is the kinematic viscosity, and indices 1 and 2 refer to the inner and the outer spheres respectively.

The case of a thin layer $\delta = 0.11$ and both spheres rotating is considered in this paper, with the main purpose being to simulate numerically three-dimensional oscillating secondary flows observed in the experiments. Such a gap width is chosen because of the wealth of laboratory (Yavorskaya, Belyaev & Monakhov 1977; Yavorskaya *et al.* 1980; Wimmer 1981; Nakabayashi 1983; Bartels 1982; Yavorskaya & Belyaev 1986) and numerical (Astaf'eva, Vvedenskaya & Yavorskaya 1978; Schrauf 1986) data obtained with this or nearby values of δ. A brief discussion of the previous laboratory and numerical investigations of the flow between rotating spheres appears in §1.1. Section 2 reviews the method of calculations. After a presentation of the results concerning the linear stability of the basic flow in §3, the numerical simulation of nonlinear secondary regimes and transitions among them is described in §4. A general discussion is given in the concluding section.

1.1. *Review of previous results*

Numerous experimental and numerical studies have been undertaken in concentric spherical annuli since Taylor vortices were discovered in these by Khlebutin (1968). It was found that the steady basic flow is axisymmetric and reflection-symmetric and consists of differential rotation about the axis and circulation in the meridional plane. The basic meridional flow depends on parameters of the problem (Yavorskaya & Belyaev 1986) and, generally, takes the form of relatively weak (in the case of a thin gap) horizontal vortices, extending from the poles to the equator.

For the most part the previous experimental and numerical studies of spherical Couette flow were devoted to the case of a fixed outer sphere ($Re_2 = 0$). The following brief survey is restricted to the results concerning the flow in 'small-gap' geometries, i.e. those with Taylor vortices developing at the stability limit of the basic flow. The upper bound of this region can be defined from the experiments by Khlebutin (1968), Wimmer (1977), and Belyaev *et al.* (1980) as $\delta = 0.19$.

By increasing the Reynolds number Re_1, Khlebutin (1968), Wimmer (1976), and others observed in experiments the first instability of the basic flow as a transition to the flow with one pair of Taylor vortices at the equator. This steady secondary flow is axisymmetric and reflection-symmetric. The transition back to the basic flow occurs if the Reynolds number is reduced. The numerical study by Schrauf (1986) has shown that there is a hysteresis in this transition, with its magnitude diminishing rapidly with δ.

Many more flow modes were observed in the supercritical region (Yavorskaya *et al.* 1977; Bühler & Zierep 1984; Yavorskaya & Belyaev 1986; Nakabayashi 1983; Nakabayashi & Tsuchida 1988*a*, *b*). There are modes with more than one pair of Taylor vortices, with wavy or spiral vortices, etc. An intriguing stable steady axisymmetric flow with one pair of Taylor vortices which is equatorially asymmetric was discovered by Bühler (1990) and thoroughly explored in the recent paper by Mamun & Tuckerman (1995).

Extensive experimental studies of secondary flows and transition to turbulence in

the flow with $\delta = 0.1096$ and both boundary spheres rotating were conducted by Yavorskaya *et al.* (1977, 1980), and Yavorskaya & Belyaev (1986). It was shown that the transition to the flow with one pair of Taylor vortices occurs at the stability limit of the basic flow only in a restricted range of the outer-sphere angular velocity, that is, in the range $-920 < Re_2 < 1940$. Outside this range at $1940 < Re_2 < 4290$ the primary bifurcation breaks the rotational symmetry, with the instability resulting in the formation of a three-dimensional azimuthally travelling wave flow with spiral vortices originating at the equator. At smaller Re_2 this flow exists at supercritical values of Re_1 and can be obtained experimentally by transition from other secondary regimes or by fast acceleration of the boundary spheres. Rotation of the boundary spheres in opposite directions leads for $-3350 < Re_2 < -920$ to a first instability in the form of azimuthally travelling spirals which differ significantly from those mentioned above in their spatial structure. It can be assumed that there is a similarity between this flow and the spiral vortices observed as a first secondary state in the Couette flow between counter-rotating cylinders (Coles 1965; Krueger, Gross & DiPrima 1966; Andereck, Liu & Swinney 1986; Langford *et al.* 1988). At $Re_2 > 4290$ or $Re_2 < -3350$ transitions to other three-dimensional non-steady secondary flows were detected in experiments.

As far as we know, almost all the previous numerical studies of SCF have been restricted to the axisymmetric case. The exceptions were presented by Dumas & Leonard (1994) and Dumas (1994). The secondary spiral-vortex flow observed by Nakabayashi (1983) in a narrow gap with $\delta = 0.06$ and $Re_2 = 0$ was simulated numerically in the first work. The numerical results discussed in the second paper concern the first instability of the basic flow in wide layers with $\delta > 0.33$ (the so-called 'wide-gap instability'), which was observed in experiments by Belyaev, Monakhov & Yavorskaya (1978) to result in transition into a three-dimensional secondary flow.

Nowadays the transitions among the steady axisymmetric secondary flows with one and two pairs of Taylor vortices and the basic flow in the layers with $\delta < 0.19$ and $Re_2 = 0$ are most clearly understood. As shown by Marcus & Tuckerman (1987) and Astaf'eva (1985*a*, *b*), the basic flow loses stability at $Re_1 = Re_{1c}(\delta)$ to an axisymmetric, anti-reflection symmetric linear mode. These authors and Schrauf (1986) have defined this as a symmetry-breaking pitchfork bifurcation, at which branches of unstable equatorially asymmetric solutions bifurcate. The time evolution of the solutions results in transition to the secondary flow with one pair of Taylor vortices. The transition back to the basic flow at a slightly lower Reynolds number can be identified with a turning point of the branch of Taylor vortex flow (Schrauf 1986). A careful study of the secondary flow with two pairs of Taylor vortices conducted by Marcus & Tuckerman (1987) for the layer with $Re_2 = 0$ and $\delta = 0.18$ revealed that this flow and the basic one are part of the same equilibrium family.

The present investigation is believed to be the first extensive study to simulate numerically three-dimensional non-steady secondary regimes of SCF in thin layers. Attention will be concentrated on the azimuthally travelling wave flows observed in the experiments by Yavorskaya *et al.* (1977, 1980) and Yavorskaya & Belyaev (1986). The gap size $\delta = 0.11$ and the outer sphere angular velocity within the range $-1300 \leqslant Re_2 \leqslant 2500$ are chosen for the investigation.

2. Equations and method of solution

2.1. *Governing equations*

We solve the Navier–Stokes equations for incompressible fluid:

$$\frac{\partial \boldsymbol{U}}{\partial t} + (\boldsymbol{U}\cdot\nabla)\boldsymbol{U} = -\nabla P + \frac{1}{Re_1}\nabla^2 \boldsymbol{U}, \tag{2.1}$$

$$\nabla\cdot\boldsymbol{U} = 0, \tag{2.2}$$

where $\boldsymbol{U}$ is the velocity field and P is the pressure. A standard spherical coordinate system (r,θ,φ) with *radial*, *polar* and *azimuthal* directions is used. The no-slip boundary conditions at the inner and outer radii are

$$\boldsymbol{U}(r=1,\theta,\varphi,t) = \boldsymbol{e}_\varphi \sin\theta, \tag{2.3a}$$

$$\boldsymbol{U}(r=1+\delta,\theta,\varphi,t) = \boldsymbol{e}_\varphi \omega(1+\delta)\sin\theta, \tag{2.3b}$$

where

$$\omega = \Omega_2/\Omega_1, \qquad \boldsymbol{U} = u\boldsymbol{e}_r + v\boldsymbol{e}_\theta + w\boldsymbol{e}_\varphi, \qquad (\boldsymbol{U}\cdot\nabla)\boldsymbol{U} = F^u\boldsymbol{e}_r + F^v\boldsymbol{e}_\theta + F^w\boldsymbol{e}_\varphi.$$

Finally, regularity conditions at the poles are required.

In (2.1)–(2.3) the values $R_1, 1/\Omega_1, R_1\Omega_1$ and $\rho R_1^2\Omega_1^2$ are used as length, time, velocity, and pressure scales respectively.

2.2. *Numerical representation*

The numerical method we use is a modification of one developed by Yavorskaya, Vvedenskaya & Astaf'eva (1978) and Astaf'eva (1985*a*, *b*). Any steady or time-periodic flow is found as the limit at $t\to\infty$ of the solution to the initial-boundary value problem consisting of (2.1)–(2.3) and initial condition

$$\boldsymbol{U}(r,\theta,\varphi,t=t_0) = \boldsymbol{U}_0(r,\theta,\varphi), \tag{2.4}$$

where $\boldsymbol{U}_0$ is generally taken to be the flow calculated at nearby values of the parameters or, in specific cases, the Stokes solution (2.7). A combined method (spectral decomposition in polar and azimuthal directions and finite-difference technique in radial direction) is used.

A solenoidal velocity field in a spherical layer can be represented as a sum of toroidal and poloidal terms (see Joseph 1976, App. B6, pp. 233–237)

$$\boldsymbol{U} = \mathrm{rot}(\boldsymbol{e}_r T(r,\theta,\varphi,t)) + \mathrm{rot}^2(\boldsymbol{e}_r S(r,\theta,\varphi,t)) \tag{2.5}$$

without loss of generality. The expansions of the unknown functions T, S, and P are constructed in such a way as to satisfy all the boundary and geometry conditions: no-slip conditions on the walls, periodicity in the φ-direction and regularity at the poles. The first step is to decompose the velocity field into two components

$$\boldsymbol{U} = \boldsymbol{U}^h + \boldsymbol{U}^{St}, \tag{2.6}$$

where $\boldsymbol{U}^h$ satisfies homogeneous boundary conditions on the spherical walls, while $\boldsymbol{U}^{St}$ is the time-independent solenoidal Stokes solution constructed to satisfy the actual no-slip conditions. The Stokes solution (Kotschin, Kibel & Rose 1955, §II.22, pp. 352–354)

$$\boldsymbol{U}^{St} = (0,0,w^{St}), \qquad w^{St} = (Ar + Br^{-2})\sin\theta, \tag{2.7}$$

where

$$A = \frac{\omega(1+\delta)^3 - 1}{(1+\delta)^3 - 1}, \qquad B = \frac{(1-\omega)(1+\delta)^3}{(1+\delta)^3 - 1},$$

is the solution to (2.1)–(2.3) in the Stokes limit $Re_1, Re_2 \to 0$. This solution is axisymmetric, reflection-symmetric and purely azimuthal in direction. The angular velocity of the flow $w^{St}/r\sin\theta$ is independent of θ. With the toroidal–poloidal representation (2.5) the Stokes solution can be rewritten as

$$S^{St} = 0, \qquad T^{St} = (Ar^2 + Br^{-1})\cos\theta. \tag{2.8}$$

At small Re_1 and Re_2 the basic flow in thin layers is still mostly azimuthal and does not depart greatly from the Stokes flow. In particular, in the parameter range considered in the present paper ($\delta = 0.11, -1300 \leqslant Re_2 \leqslant 2500$, and Re_1 near the critical value Re_{1c} of linear stability of the basic flow) the Stokes term in (2.6) contains most of the flow energy.

The spherical harmonics $Y_l^m(\theta,\varphi) = P_l^m(\cos\theta)e^{im\varphi}$ (P_l^m is an associated Legendre function) are used to expand the unknown part $\boldsymbol{U}^h$ of the velocity field and the pressure P (superscript 'h' is omitted below):

$$\{T, S, P\}(r,\theta,\varphi,t) = \sum_{l,m}\{T_{lm}, S_{lm}, H_{lm}\}(r,t)Y_l^m(\theta,\varphi). \tag{2.9}$$

The spherical harmonics are chosen since they are periodic in φ, satisfy the regularity condition at the poles and are the natural orthogonal basis functions for a spherical geometry, in that they are the eigenfunctions of the θ–φ part of the Laplacian. What is more, they do not display the 'pole problem' which plagues Fourier series and finite-difference schemes in polar angle (Orszag 1974).

The series are truncated so that $|m| \leqslant M$, $|m| \leqslant l \leqslant L$. The restriction $M = 0$ is applied for axisymmetric solutions. As seen from the experimental results by Yavorskaya *et al.* (1977, 1980) and Yavorskaya & Belyaev (1986), all non-axisymmetric flows considered here have large azimuthal scale, i.e. the fundamental azimuthal wavenumber is something like one or two. Therefore, with the goal of reducing the amount of calculation, the value of M is no more than $M = 6$. Note that generally we are not imposing the restriction of reflection-symmetry on the θ-expansion of the velocity and pressure fields. This means that we include all terms in (2.9), and not just the terms with $l-m$ odd in the T-expansion and $l-m$ even in the other expansions.

The substitution of the expansion (2.9) into (2.1) and the application of the operators

$$\boldsymbol{e}_r \cdot \mathrm{rot}, \qquad \boldsymbol{e}_r, \quad \text{and} \quad -(\sin\theta)^{-1}\left(\frac{\partial}{\partial\varphi}\boldsymbol{e}_\varphi + \frac{\partial}{\partial\theta}\sin\theta\boldsymbol{e}_\theta\right)$$

yield the following equations for the complex-valued coefficients T_{lm}, S_{lm} and H_{lm}:

$$\sum_{l,m}\left[\frac{\partial T_{lm}}{\partial t} + \frac{1}{Re_1}D_l(T_{lm})\right]Y_l^m\frac{l(l+1)}{r} = \left[\frac{\partial F^v}{\partial\varphi} - \frac{\partial}{\partial\theta}(\sin\theta F^w)\right]\frac{1}{\sin\theta} = \Phi^T, \tag{2.10a}$$

$$\sum_{l,m}\left[\frac{\partial S_{lm}}{\partial t} + \frac{1}{Re_1}D_l(S_{lm}) + \frac{r^2}{l(l+1)}\frac{\partial H_{lm}}{\partial r}\right]Y_l^m\frac{l(l+1)}{r^2} = -F^u = \Phi^S, \tag{2.10b}$$

$$\sum_{l,m}\left[\frac{\partial Q_{lm}}{\partial t} + \frac{1}{Re_1}\left(D_l(Q_{lm}) - \frac{2l(l+1)}{r^2}S_{lm}\right) + H_{lm}\right]Y_l^m\frac{l(l+1)}{r}$$
$$= \left[\frac{\partial F^w}{\partial\varphi} + \frac{\partial}{\partial\theta}(\sin\theta F^v)\right]\frac{1}{\sin\theta} = \Phi^Q, \tag{2.10c}$$

where

$$D_l = \frac{l(l+1)}{r^2} - \frac{\partial^2}{\partial r^2}, \qquad Q_{lm} = \frac{\partial S_{lm}}{\partial r}.$$

The new field Q_{lm} is defined to eliminate third- and fourth-order radial derivatives from the equations. The boundary conditions are

$$T_{lm} = S_{lm} = Q_{lm} = 0 \quad \text{at} \quad r = 1, \quad 1+\delta. \tag{2.11}$$

Now consider the nonlinear right-hand sides of equations (2.10). It is shown in Appendix A that each of them can be expanded in a finite series of spherical harmonics:

$$(\Phi^T, \Phi^S, \Phi^Q) = \sum_{m=-2M}^{2M} \sum_{l=|m|}^{2L} (f^T_{lm}, f^S_{lm}, f^Q_{lm}) Y_l^m. \tag{2.12}$$

The coefficients for $0 \leqslant m \leqslant M$ and $m \leqslant l \leqslant L$ are calculated at each time step by means of the following procedure.

The expansion in $e^{im\varphi}$ is produced by straightforward evaluation of convolution sums. The employment of this procedure instead of the fast Fourier transform is justified by the small value of M. A pseudo-spectral technique is applied to the polar direction. We compute the velocity field components at the nodes of Gaussian quadrature, perform the nonlinear multiplications and transform back to the spectral space via Gauss-type integration. In view of (2.12) the appropriate integrals can be written in the form

$$\int_{-1}^{1} P_k^m \sum_{l=|m|}^{2L} f_{lm} P_l^m \mathrm{d}\mu,$$

where $\mu = \cos\theta$ and f_{lm} stands for f^T_{lm}, f^S_{lm} or f^Q_{lm}. The products $P_k^m P_l^m$ are polynomials in μ of degree not exceeding $3L$. Therefore, Gauss integration is performed to machine accuracy provided the degree of the Legendre polynomial used for the quadrature is greater than or equal to $(3L+1)/2$.

In our calculations the pseudospectral procedure was realized in the following manner. First, the coefficients F^u_m, F^v_m and F^w_m of the expansion in $e^{im\varphi}$ are computed at the quadrature nodes,

$$F^u(r,\theta,\varphi,t) = \sum_{m=-M}^{M} F^u_m(r,\theta,t) e^{im\varphi}, \ldots. \tag{2.13}$$

Then the formulas

$$\left.\begin{aligned} f^T_{lm} &= \int_{-1}^{1} \left(F^v_m \frac{im}{\sin\theta} P_l^m + F^w_m \frac{\partial P_l^m}{\partial \theta} \right) \mathrm{d}\mu, \\ f^S_{lm} &= -\int_{-1}^{1} F^u_m P_l^m \mathrm{d}\mu, \\ f^Q_{lm} &= \int_{-1}^{1} \left(F^w_m \frac{im}{\sin\theta} P_l^m - F^v_m \frac{\partial P_l^m}{\partial \theta} \right) \mathrm{d}\mu \end{aligned}\right\} \tag{2.14}$$

are applied. They can be obtained directly from right-hand sides of (2.10) using the relation

$$\int_{-1}^{1} \frac{1}{\sin\theta} \frac{\partial}{\partial\theta} (\sin\theta F) P_l^m \mathrm{d}\mu = -\int_{-1}^{1} F \frac{\partial P_l^m}{\partial \theta} \mathrm{d}\mu.$$

The calculations are reduced if we employ only the positive (or negative) half of quadrature nodes which are the zeros of an even polynomial. In this case, each coefficient in the expansion (2.13) should be computed as a sum of parts which are even and odd in μ. Either one or the other appears in (2.14) depending on the parity of P_l^m or $\partial P_l^m/\partial\theta$.

The uncoupled systems of four differential equations second-order in r, first-order in t for $T_{lm}(r,t)$, $S_{lm}(r,t)$, $Q_{lm}(r,t)$, and $H_{lm}(r,t)$ are solved by a technique explicit-implicit in t, finite-difference in r. In the radial direction the equations are discretized by central differences of the second order. The unknowns T_{lm}, S_{lm} and Q_{lm} are computed at the integer discretization points $r_j = 1 + j\delta/(K+1)$ $(1 \leqslant j \leqslant K)$ and the pressure H_{lm} is calculated at the half-integer points $r_{j-1/2} = 1 + (j - 1/2)\delta/(K+1)$ $(1 \leqslant j \leqslant K+1)$. Equations (2.10) are approximated at the integer points, and the equation

$$Q_{lm} - \frac{\partial S_{lm}}{\partial r} = 0$$

is approximated at the half-integer ones. The nonlinear terms are computed at the nth time layer and the other terms are computed at the $(n+1)$th one. The boundary-value difference problems are solved by a simple and convenient variant of Gauss elimination known as the 'double sweep method' (Godunov & Ryabenki 1964, §4.3, pp. 146–154).

When performing most of our numerical simulation of two- and three-dimensional flows and transitions among them, we used the following values of discretization parameters: $M = 6$ ($M = 0$ if axisymmetry is imposed); $L = 60$; $K = 10$; $\Delta t = \pi/50$=inner sphere rotation period/100. In special cases the changes in the flow structure required L, K and Δt to be changed respectively to 90, 15 and $\pi/100$. The effect of the discretization on the accuracy of calculations is discussed in Appendix B, along with the comparison of our results with the known experimental data.

The following functions are used to display the properties of the calculated axisymmetric flows:

(i) meridional streamfunction $\Psi(r,\theta,t) = -\sin\theta\partial S/\partial\theta$ such that

$$u = \frac{1}{r^2\sin\theta}\frac{\partial\Psi}{\partial\theta}, \qquad v = -\frac{1}{r\sin\theta}\frac{\partial\Psi}{\partial r};$$

(ii) angular velocity of the flow $\Omega(r,\theta,t) = w/r\sin\theta$;

(iii) polar spectrum of radial velocity, that is, the absolute value $|\, u_l(r_j)\,|$ as a function of l, where $u_l(r_j) = l(l+1)r_j^{-2}S_{l0}(r_j)$, with r_j the mid-gap radius;

(iv) torques $\tau_1(t)$ and $\tau_2(t)$ exerted by the fluid on the inner and outer spheres which are calculated by the formula

$$\begin{aligned}\tau_i(t) &= (-1)^i\frac{3}{8\pi}R_i^3\int_0^{2\pi}\int_0^{\pi}\sin^2\theta\left(\frac{\partial w}{\partial r} - \frac{w}{r}\right)\Big|_{r=R_i}\mathrm{d}\theta\mathrm{d}\varphi \\ &= (-1)^i R_i^3\left(\frac{1}{r}\frac{\partial T_{10}}{\partial r} - \frac{2T_{10}}{r^2}\right)\Big|_{r=R_i} \qquad (i=1,2),\end{aligned} \tag{2.15}$$

where $R_1 = 1$ and $R_2 = 1 + \delta$ are the dimensionless radii of boundary spheres.

If the flow is steady, then τ_1 and τ_2 are independent of time and must obey the equation

$$\tau_1 + \tau_2 = 0 \tag{2.16}$$

which follows from the time-independence of the fluid angular momentum. These

criteria are taken as evidence of completion of transition and establishment of steady-state flow after each change of parameters.

A distinctive property of travelling wave flows is that their integral characteristics such as the torques τ_1 and τ_2, the overall angular momentum of the fluid and the energy of fluid motion are independent of time. Therefore, after each parameter change we can determine the completion of the transitional process and the establishment of the new travelling wave flow by the fulfillment of the same criteria as for axisymmetric flows. It can be easily shown that (2.15) and (2.16) are suitable for travelling wave flows.

An especially acute problem arising during the numerical simulation of three-dimensional flows is the choice of technique for representing the results of calculations. Our choice is dictated by the experimental observation that in the parameter range considered here three-dimensional flows are exclusively azimuthally travelling wave flows with spiral vortices. It seems reasonable to depict vortex boundaries as curves $v = 0$ in the spherical section at a definite radius. Examples are in figures 11 and 15. Another possible way, which is to exhibit meridional velocity fields in sections at constant values of φ, is also employed in the present paper (figures 12 and 16).

With the velocity representation (2.5)–(2.9) and the well-known orthogonality properties of toroidal and poloidal fields (Chandrasekhar 1961, §129, pp. 623–626) and of spherical harmonics, the dimensionless energy of the flow can be written

$$E = \sum_{m=0}^{M} (E_m^s + E_m^a), \tag{2.17}$$

$$E_m^s = a_m \int_1^{1+\delta} \left({\sum}' b_l (b_l r^{-2} S_{lm}^2 + Q_{lm}^2) + {\sum}'' b_l T_{lm}^2 \right) \mathrm{d}r,$$

$$E_m^a = a_m \int_1^{1+\delta} \left({\sum}'' b_l (b_l r^{-2} S_{lm}^2 + Q_{lm}^2) + {\sum}' b_l T_{lm}^2 \right) \mathrm{d}r,$$

where

$$b_l = l(l+1), \qquad a_0 = 1, \quad \text{and} \quad a_m = 2 \quad \text{if} \quad m > 0,$$

$${\sum}' = \sum_{l-m=\text{even}}, \qquad {\sum}'' = \sum_{l-m=\text{odd}}.$$

In these formulas E_m^s (E_m^a) is the overall energy of reflection-symmetric (anti-reflection symmetric) velocity components with azimuthal wavenumber m. In such a manner we can construct the energy spectra shown in figures 13 and 17.

2.3. *Eigenvalues and eigenmodes*

The technique applied to calculate the eigenmodes and eigenvalues of axisymmetric equilibrium solutions is a slight modification of the initial-value code described above. Let $\boldsymbol{U}$ denote the velocity of the equilibrium, whose stability is examined. The linearized Navier–Stokes equations for the perturbations $\boldsymbol{u}$, p are

$$\frac{\partial \boldsymbol{u}}{\partial t} + (\boldsymbol{u}\cdot\nabla)\boldsymbol{U} + (\boldsymbol{U}\cdot\nabla)\boldsymbol{u} = -\nabla p + \frac{1}{Re_1}\nabla^2 \boldsymbol{u}, \tag{2.18}$$

$$\nabla \cdot \boldsymbol{u} = 0. \tag{2.19}$$

The boundary and initial conditions are

$$\boldsymbol{u} = 0 \quad \text{at} \quad r = 1, \quad 1 + \delta, \tag{2.20}$$

$$\boldsymbol{u}(r, \theta, \varphi, t = t_0) = \boldsymbol{u}_0(r, \theta, \varphi), \tag{2.21}$$

where the initial velocity field $\boldsymbol{u}_0$ is generally the eigenmode obtained with neighbouring parameter values. The initial boundary value problem (2.18)–(2.21) is then solved in the same manner as the fully nonlinear problem except that the right-hand sides of the equations are now the linear functions relative to the unknown variables. The values of parameters L and K used are identical to those for the nonlinear problem. The coefficients of the equations are independent of φ and reflection-symmetric. Therefore, we can consider separately the linear modes with different values of the azimuthal wavenumber m and with different equatorial symmetry. This enables a reduced series of spherical functions to be used for expanding the perturbations. For example, the reflection-symmetric linear mode with wavenumber m can be expanded as

$$\{S, p\}(r, \theta, \varphi, t) = \sum_{l}' \{S_{lm}, h_{lm}\}(r, t) Y_l^m(\theta, \varphi),$$

$$\{T\}(r, \theta, \varphi, t) = \sum_{l}'' \{T_{lm}\}(r, t) Y_l^m(\theta, \varphi).$$

By evolving (2.18)–(2.19) forward in time, $\boldsymbol{u}$ converges to the eigenmode which is preferred (most unstable or least stable) among the eigenmodes with a given m and type of equatorial symmetry. The eigenvalue of the preferred mode is determined in the following manner.

The coefficients

$$\alpha_{lj}^m(t) + \mathrm{i}\beta_{lj}^m(t) = \frac{1}{T_{lm}} \frac{\partial T_{lm}}{\partial t}, \qquad \gamma_{lj}^m(t) + \mathrm{i}\sigma_{lj}^m(t) = \frac{1}{S_{lm}} \frac{\partial S_{lm}}{\partial t} \tag{2.22}$$

are calculated after each time step for each $l = m, \ldots, L$ at every discretization point r_j. All the coefficients converge to the eigenvalue $\lambda^m + \mathrm{i}\omega^m$ of the preferred mode as $t \to \infty$. The computations are interrupted when $\alpha_{lj}^m + \mathrm{i}\beta_{lj}^m$ and $\gamma_{lj}^m + \mathrm{i}\sigma_{lj}^m$ for all l and j coincide to the fourth decimal place.

In the parameter range under consideration all the preferred non-axisymmetric modes were found to be azimuthally travelling waves, with the wave speed $W = -\omega^m/m$ being of the order of the inner-sphere angular velocity. At not-too-small m the large value of oscillation frequency ω^m causes the required time step Δt to be substantially reduced in comparison with that for the axisymmetric mode. This complication can be circumvented by going into the rotating frame

$$T_{lm}(r, t) = \mathrm{e}^{-\mathrm{i}mW^* t} T_{lm}^*(r, t), \quad \text{etc.} \tag{2.23}$$

where W^* is the wave speed of the mode calculated with neighbouring parameter values. The equations in unknowns $T_{lm}^*, S_{lm}^*, Q_{lm}^*$ and H_{lm}^* differ from those in T_{lm}, S_{lm}, Q_{lm} and H_{lm} only in the time-derivative term

$$\frac{\partial T_{lm}}{\partial t} = \mathrm{e}^{-\mathrm{i}mW^* t} \left(-\mathrm{i}mW^* T_{lm}^* + \frac{\partial T_{lm}^*}{\partial t} \right), \quad \text{etc.} \tag{2.24}$$

The extra terms $\mathrm{i}mW^* T_{lm}^*, \ldots$ are computed at the nth time layer. The new solution components $\{T_{lm}^*, S_{lm}^*, Q_{lm}^*, H_{lm}^*\}$ oscillate with small frequency $m(W^* - W)$. Therefore, we can use the same time step $\Delta t = \pi/100$ as for the axisymmetric mode. A similar

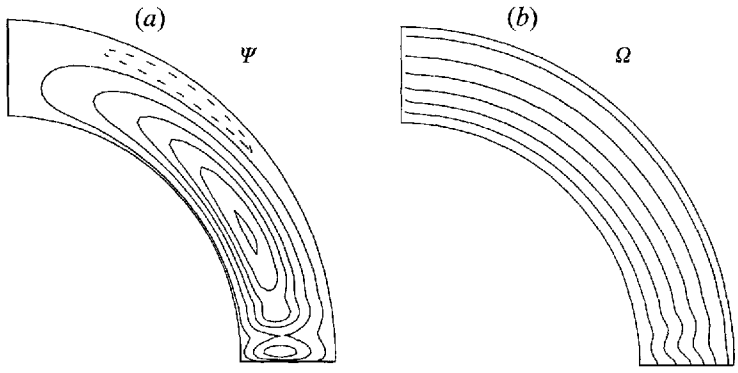

FIGURE 1. The basic flow with additional vortices and pinches. $Re_2 = -1200$, $Re_1 = 1597.3 = Re_{1c}(Re_2)$. Radius r is mapped linearly from the interval $[1, 1+\delta]$ to $[1, 1.4]$ and only the upper hemisphere is plotted. (*a*) Streamlines of the meridional flow. The large vortex (solid contours) rotates in a counterclockwise direction and the additional small vortex (dashed contour) rotates in a clockwise direction. The solid contours are drawn with the values of streamfunction Ψ equally spaced between -1.5×10^{-4} and -9×10^{-4} and the dashed contour is drawn with $\Psi = 10^{-5}$. (*b*) Contours of constant angular velocity. The values of Ω are equally spaced between -0.6 (outer sphere) and 1 (inner sphere). Wiggles near the equator are due to the pinch.

expedient is applied when solving the fully nonlinear problem for travelling wave flows.

3. Linear stability of the basic flow

3.1. *Basic flow*

The basic flow consists of a differential rotation about the axis and a meridional circulation which is induced by Ekman pumping at the poles and is composed of one or two large vortices in each hemisphere. The number of vortices and the direction of their circulation are determined by the parameters of the problem.

Ovseenko (1963) developed an expansion of the solution in powers of Re_1. It was shown by Munson & Joseph (1971) and verified by our calculations for the case of a thin layer that the series converges very slowly and, therefore, can be used only at small Reynolds numbers. Only a numerical simulation can give a correct description of the structure of the basic flow near the stability limit.

Our calculations have shown that in most of the parameter range considered here the meridional part of the basic flow consists of one large vortex in each hemisphere. The vortices rotate in opposite directions in such a way that the flow at the equator is always directed from the inner sphere to the outer one. The flow is reflection-symmetric. If Re_2 is decreased into the region of strong counter-rotation, a basic meridional flow of another type appears, that is, an additional vortex develops near the pole and the outer sphere in each hemisphere. A typical example of such a flow is shown in figure 1.

The demarcation curve between the two types of basic flow passes in the (Re_2, Re_1)-plane from the origin to the point of intersection with the linear stability curve $Re_1 = Re_{1c}(Re_2)$ at $Re_2 = -940$. Near the origin the curve is an almost straight line $Re_2/Re_1 = \text{const} < 0$ (cf. Yavorskaya *et al.* 1980; Yavorskaya & Belyaev 1986). In the region $Re_2 > -1300$ considered here, the additional vortices are very weak and far from the equator. Since in the present paper we focus on the formation of Taylor

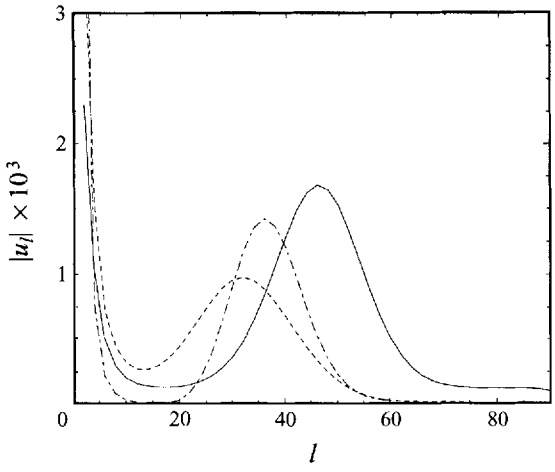

FIGURE 2. Polar spectra of the radial velocity of the pinched basic flows calculated at the stability limit. ——, $Re_2 = -1200$; — · — · —, $Re_2 = 0$; — — — —, $Re_2 = 2050$. The curves are drawn through the discrete sets of points; the coefficients u_l are non-zero when l is even. Each spectrum has two local maxima, the second one corresponding to the pinch and disappearing when Re_1 is decreased.

and spiral vortices near the equator, these additional vortices are likely to have little influence on the phenomena under study.

Another feature of the flow shown in figure 1 is the pinching of meridional streamlines. The pinching was investigated numerically by Bonnet & Alziary de Roquefort (1976), Marcus & Tuckerman (1987), and Bar-Yoseph *et al.* (1990) for the case $Re_2 = 0$. It was found by our calculations that the pinches develop in the flow at Re_1 just less than Re_{1c} everywhere over the region $-1300 \leqslant Re_2 \leqslant 2500$. Calculations carried out with different values of the truncation parameter L ($L = 20, 30, 60, 90, 110$) have demonstrated that the minimum value of L that provides an adequate reproduction of the basic flow with pinches is $L = 60$ or $L = 90$ depending on Re_2. As an illustration, figure 2 shows the polar spectra of the radial velocity of different pinched basic flows. The spectra display two local maxima which are the wavenumbers associated with the large basic vortex and the pinch.

3.2. *Linear stability problem*

A search for the most unstable linear mode requires the computation of stability of the basic flow relative to axisymmetric and first nine non-axisymmetric modes. The reflection-symmetric and anti-reflection-symmetric modes are considered separately. The results have been detailed in Zikanov (1993*a*, *b*, 1995). Only a brief discussion will be given here.

Figure 3 shows the critical number Re_{1c} of the basic flow stability as a function of Re_2. The linear stability problem demonstrates the diversity of symmetry-breaking bifurcations of spherical Couette flow in the range of Re_2 under consideration. This range can be divided into three parts.

When $-646 < Re_2 < 1811$, the first instability of the basic flow is to an eigenmode that is axisymmetric and anti-reflection-symmetric. In this region the primary bifurcation of the basic flow breaks the equatorial reflection symmetry, with the rotational symmetry remaining unchanged. The eigenvalue of the preferred eigenmode is always real. As pointed out below, this instability induces a transition to the secondary flow with one pair of Taylor vortices.

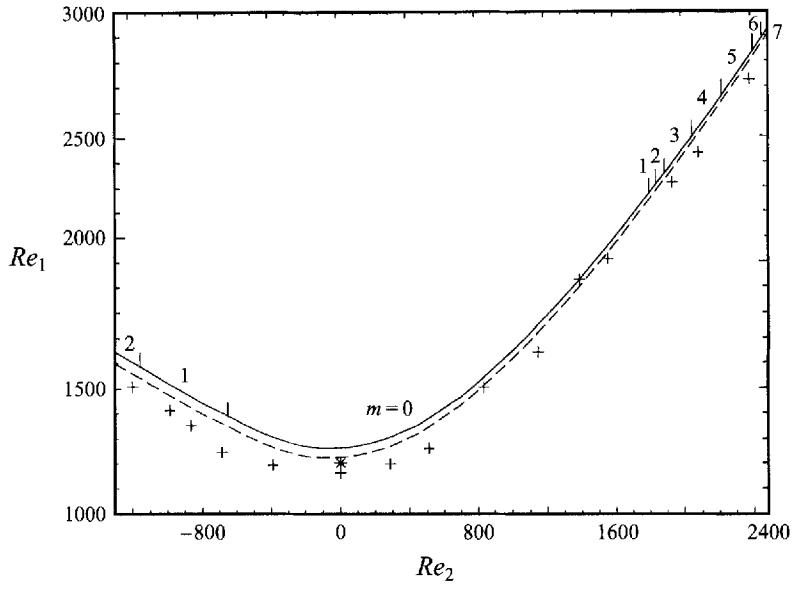

FIGURE 3. ———, Critical number Re_{1c} of stability of the basic flow as a function of Re_2; m, the azimuthal wavenumber of the preferred eigenmode; — — — —, experiments with $\delta = 0.1096$, the lower boundary of the region of existence of secondary flows (Yavorskaya *et al.* 1977, 1980; Yavorskaya & Belyaev 1986); + + +, experiments with $\delta = 0.111$, the critical numbers for transition to the flow with one pair of Taylor vortices (Wimmer 1981); *, point of the equatorial symmetry-breaking bifurcation of the basic flow calculated by Schrauf (1986) for $\delta = 0.115$ and $Re_2 = 0$.

At $1811 < Re_2 < 2500$ the preferred eigenmodes are also anti-reflection-symmetric. In addition, they are non-axisymmetric, that is, the primary bifurcation breaks the rotational symmetry as well as the equatorial one. The preferred mode number changes consequently from $m = 0$ to $m = 1$ and then to $m = 2, 3, 4, 5, 6, 7$. The apparent smoothness of this part of the stability curve at the points of change of m can be explained through figure 4. The slopes of the two intersecting curves $Re_1^m(Re_2)$ of stability to the modes with neighbouring values of m differ little from one another at such points.

In line with the theoretical results by Ruelle (1973), the non-axisymmetric modes are azimuthally travelling waves. The imaginary part of the eigenvalue of the preferred eigenmode is always negative. What this means is that the travelling waves propagate in the sense of rotation of the inner sphere. It will be shown in §4.2 that this instability results in transition to the travelling wave flow with spiral vortices.

When the boundary spheres rotate in opposite directions and $-1300 < Re_2 < -646$, a third type of symmetry-breaking bifurcation appears. Again the preferred eigenmodes are azimuthally travelling waves propagating in the sense of rotation of the inner sphere. But in this case they are reflection-symmetric. The preferred mode number is $m = 1$ when $-1112 < Re_2 < -646$ and $m = 2$ when $Re_2 < -1112$. The nonlinear simulation of secondary flows described in §4.3 gives in this region the transition to the flow with rotating spiral vortices which differ in spatial structure from those mentioned above. This part of our results can be compared with the results obtained for the Couette flow between counter-rotating cylinders. Langford *et al.* (1988) solved the linear stability problem for the cylindrical layer with $\delta = 0.1325$ and found that at $Re_2 < -1109.97$ the basic flow becomes unstable

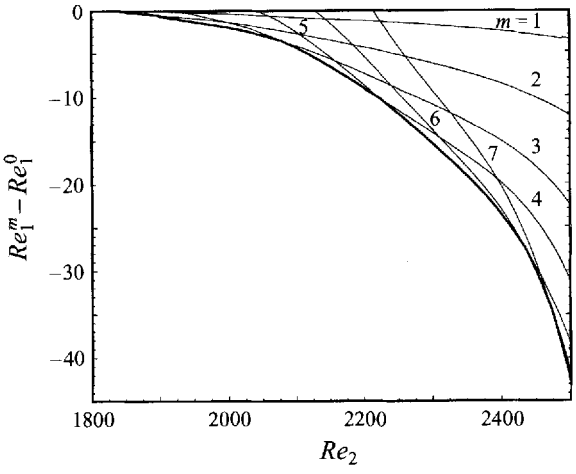

FIGURE 4. ——, Differences $Re_1^m(Re_2) - Re_1^0(Re_2)$ versus Re_2, where Re_1^m is the critical number of instability of the basic flow to mode m. ——, stability limit Re_{1c} defined for a given Re_2 by the smallest value of Re_1^m for all possible m.

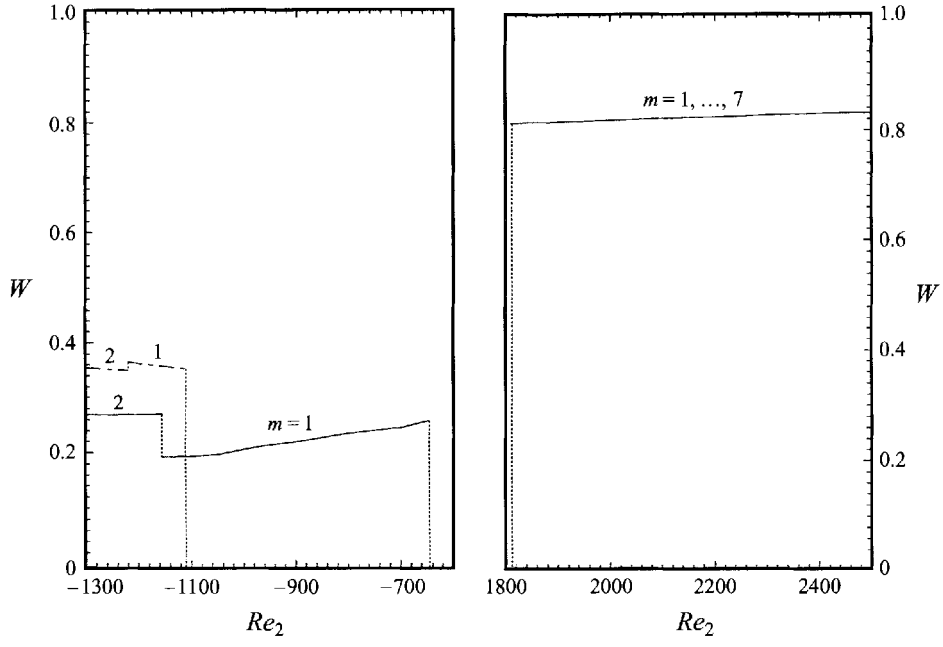

FIGURE 5. ——, Wave speed of the preferred travelling wave linear modes (in units of the angular velocity of the inner sphere); — · — · —, wave speed of preferred modes in counter-rotating cylindrical Couette flow with $\delta = 0.1325$ (Langford *et al.* 1988).

to rotating spiral vortices. Their results concerning the wave speed are depicted in figure 5 and show a qualitative agreement with our results.

Figure 5 presents the wave speed $W = -\omega^m/m$ (ω^m is the imaginary part of the eigenvalue) of preferred non-axisymmetric modes. The jumps at $Re_2 = -1112$, -646, 1811 are due to the changes of the wavenumber m from 2 to 1, from 1 to 0 and from 0 to 1. A striking feature of the plot is that there are no such jumps when $1811 < Re_2 < 2500$, even though m changes from 1 to 2 and then to $3, \ldots, 7$.

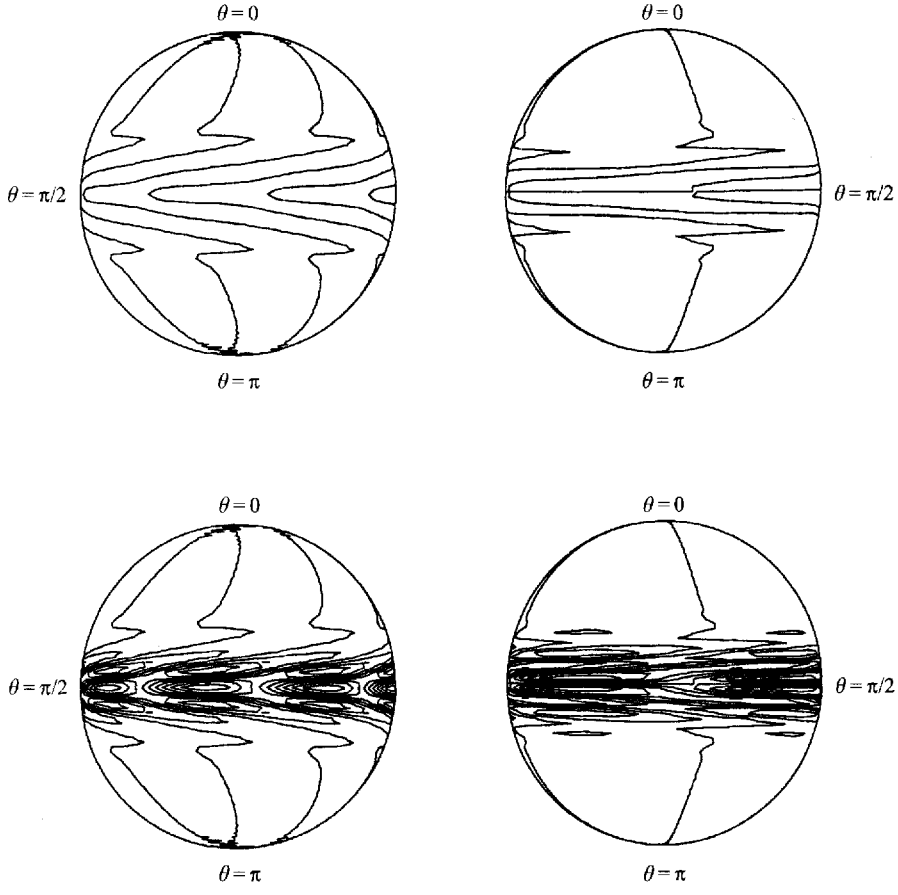

FIGURE 6. Preferred non-axisymmetric linear modes. On the left, anti-reflection-symmetric mode $m = 4$ at $Re_2 = 2050$; on the right, reflection-symmetric mode $m = 2$ at $Re_2 = -1200$. Contours of zero (top) and equally spaced constant (bottom) polar velocity component v are plotted in the spherical section at mid-gap radius projected onto the vertical plane. The vortices near the equator contain most of the flow energy.

It follows from our calculations that in this range the rotating waves are essentially dispersionless with respect to the azimuthal wavenumber. The wave speeds of different modes coincide for given Re_2 and Re_1 to the third decimal place.

Plots of non-axisymmetric preferred modes can be seen in figure 6. Three ranges of Re_2 are distinguished as discussed above, according to the different types of symmetry of the eigenvectors. When $-646 < Re_2 < 1811$ and the preferred mode is axisymmetric, the vortices are closed and are, in fact, Taylor vortices. A plot of this mode can be found, for example, in Marcus & Tuckerman (1987). In the other two ranges of Re_2 the vortices are open and, in this respect, are similar to the spiral vortices detected by our nonlinear calculations (see figures 11 and 15). The vortices are inclined to the equatorial plane and move in the azimuthal direction. At $Re_2 < -646$ the eigenvectors are reflection-symmetric, whereas at $Re_2 > -646$ this symmetry is broken and there is flow across the equator, which is forbidden in equatorially symmetric flows. The intensity of fluid motion diminishes rapidly from the equator to the poles.

The results of the linear stability analysis are in a good agreement with the

experimental observations by Wimmer (1981), Yavorskaya *et al.* (1977, 1980), and Yavorskaya & Belyaev (1986) as shown in figure 3. Three-dimensional secondary regimes were not detected at the stability limit in Wimmer's experiments. All his data shown in figure 3 correspond to the first instability of the basic flow resulting in the axisymmetric Taylor vortex flow. In contrast, in the experiments performed by Yavorskaya, Belyaev and co-workers two three-dimensional flows with spiral vortices were observed at the stability limit in the range of Re_2 considered here. The dashed curve represents the experimentally obtained lower boundary of the existence region of secondary flows. One can see that this boundary coincides very closely with the linear stability curve. There is one more point of agreement between the results of the experiments by Yavorskaya and co-workers and of the linear stability analysis. The ranges of primary bifurcation breaking the rotational symmetry are similar: $Re_2 > 1940$ and $Re_2 < -920$ for the experiments and $Re_2 > 1811$ and $Re_2 < -646$ for the present study. It would be useful to compare the calculated wave speed with the experimentally obtained one. Unfortunately, the available experimental results on the wave speed of the secondary flows considered here are rather poor. We can only mention that in experiments, as in our calculations, travelling waves propagate in the sense of rotation of the inner sphere.

4. Secondary regimes and transitions among them

This section presents the results of nonlinear simulations of experimentally detected secondary regimes which are steady axisymmetric flows with one and two vortices per hemisphere and two different non-steady three-dimensional flows with spiral vortices arising at positive and negative values of Re_2. We will refer to these flows and to the basic flow as regimes I, II, S_1, S_2, and 0, respectively. The numerical code described in §2.2 is applied to investigate the regimes and transitions among them. The linear stability of the axisymmetric secondary flows is also examined. A representative bifurcation diagram is constructed in each of the three regions $Re_2 < -646$, $-646 < Re_2 < 1811$, and $Re_2 > 1811$ determined by the linear stability analysis of the basic flow.

4.1. *Slow rotation of the outer sphere;* $-646 < Re_2 < 1811$

This region matches the one $-920 < Re_2 < 1940$ determined experimentally in Yavorskaya *et al.* (1977, 1980), and Yavorskaya & Belyaev (1986). The experimentally observed structure of secondary flows and transitions among them is represented by the well-studied case $Re_2 = 0$. The first instability of the basic flow results in transition to the flow with one pair of Taylor vortices (regime I). In the supercritical region, the flow with two pairs of Taylor vortices (regime II) and the travelling wave flow with spiral vortices (regime S_1 in our notation) can be experimentally obtained by fast acceleration of the inner sphere or both boundary spheres. Each of the two secondary flows demonstrates a transition to regime I as Re_1 is decreased through the lower boundary of the existence region. Two more steady axisymmetric and reflection-symmetric flows with three and four pairs of Taylor vortices are added to the set of secondary regimes as Re_1 is increased further into the supercritical region. It was shown in the experiments that all the flows with Taylor vortices are steady only in restricted ranges of Re_1. At larger Re_1 the flows are unstable to azimuthally travelling sinusoidal disturbances on the vortices, the instability being very similar to that observed in cylindrical Taylor–Couette flow.

The previous numerical investigations dealt for the most part with axisymmetric

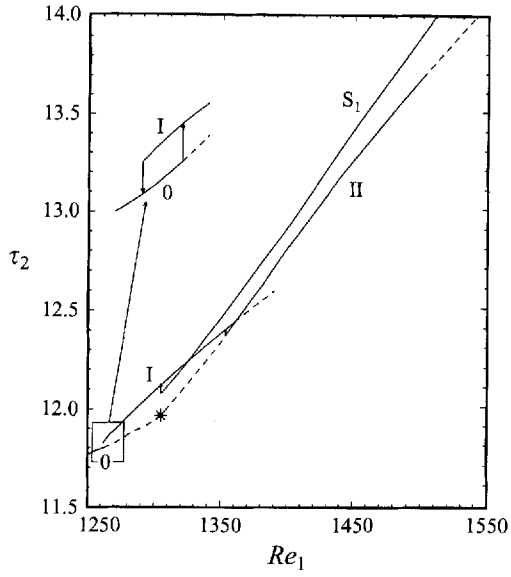

FIGURE 7. Bifurcation diagram at $Re_2 = 0$. The torque τ_2 of different flow regimes is shown as a function of Re_1. —— (– – – –), linearly stable (unstable) solutions; ↑, ↓, transitions which are possible under quasi-static change of Re_1; *, point of the smooth transformation of regime 0 to regime II. 0, I, II, and S_1 denote, respectively, the basic flow, the flows with one and two pairs of Taylor vortices and the flow with rotating spiral vortices shown in figures 11 and 12.

regimes. Regimes I and II and transitions among them and the basic flow have been most clearly understood (Schrauf 1986; Marcus & Tuckerman 1987; Astaf'eva 1985*a*, *b*; Bar-Yoseph *et al.* 1990).

Figure 7 shows the bifurcation diagram constructed as the result of our calculations at $Re_2 = 0$. The torque τ_2 exerted by two- and three-dimensional flows on the outer sphere is presented as a function of Re_1. A comparison between the computed and experimentally observed values of Re_1 for transitions among different regimes can be found in Appendix B.

When $Re_1 = Re_{1c} = 1262.5$, the basic flow equilibrium becomes unstable at an equatorial symmetry-breaking subcritical pitchfork bifurcation and a $0 \rightarrow$ I transition occurs, which is asymmetric with respect to reflection about the equator. A comprehensive analysis of this transition in the flow with $\delta = 0.18$ can be found in the paper by Marcus & Tuckerman (1987). At $Re_1 = 1261.2$ the curve of regime I has a turning point. The transition I $\rightarrow$ 0 which was also described by Marcus & Tuckerman (1987) can be initiated by lowering Re_1 to a value less than 1261.2. It breaks neither the equatorial nor the rotational symmetry. This result of nonlinear simulations is confirmed by our linear stability analysis of regime I. As Re_1 approaches the turning point, the eigenvalue of the least-stable eigenmode tends to zero, with the mode being axisymmetric and reflection-symmetric.

The hysteresis $\Delta Re_1 = Re_1^{0\rightarrow 1} - Re_1^{1\rightarrow 0}$ is very small at $Re_2 = 0$. This fact seems to be responsible for the contention by experimentalists that the bifurcation to the Taylor vortex flow is supercritical if the layer is thin (Yavorskaya *et al.* 1980). More precise experiments (Yu. N. Belyaev 1994, private communication) detected hysteresis $\Delta Re_1 = 0.7 \pm 0.25$ in the flow with $\delta = 0.1096$ and $Re_2 = 0$. This value is consistent with the value $\Delta Re_1 = 1.3$ obtained in our calculations. Agreement with the results

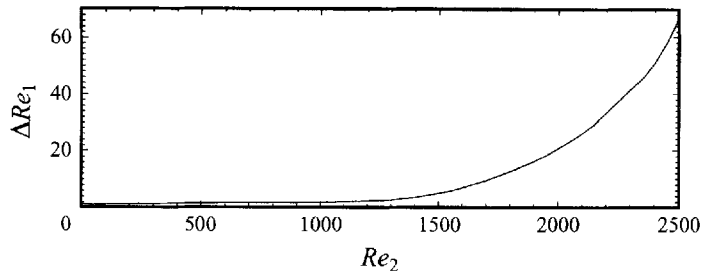

FIGURE 8. Hysteresis $\Delta Re_1 = Re_1^{0\to I} - Re_1^{I\to 0}$ of transitions between the basic flow and the flow with one pair of Taylor vortices as a function of Re_2.

of Schrauf (1986) can also be seen. He calculated $\Delta Re_1 = 1.3$ in the case of $\delta = 0.115$ and $Re_2 = 0$.

Calculations of the transitions between regimes 0 and I conducted with $0 \leqslant Re_2 \leqslant 2500$ disclose that the hysteresis depends strongly on Re_2. It can be seen in figure 8 that its magnitude increases with Re_2 up to $\Delta Re_1 = 67$ at $Re_2 = 2500$.

By imposing axial and reflection symmetry the branch of basic flow solutions can be extended into the supercritical region $Re_1 > 1262.5$ until the linear mode with both symmetries begins to grow. The extension reveals the phenomenon previously described by Marcus & Tuckerman (1987) in the flow with $\delta = 0.18$ and $Re_2 = 0$. Linearly unstable (relative to anti-reflection-symmetric modes with $m = 0$ and $m = 1$) regime 0 transforms smoothly into unstable (in the same manner) regime II. At $Re_1 = 1305 \pm (0.5)$ an additional small recirculation vortex appears in each hemisphere at the stagnation point of the pinched meridional basic flow. The intensity and the size of the vortex pair grow with Re_1. The linear stability analysis reveals that at $Re_1 = 1354.8$, regime II becomes stable. The eigenvalue of the most unstable eigenmode becomes negative, with the eigenmode being axisymmetric and anti-reflection-symmetric. At this point, which is clearly the point of an equatorial symmetry-breaking pitchfork bifurcation, decrease in Re_1 produces a transition II $\rightarrow$ I. A similar transition was described by Marcus & Tuckerman (1987).

The main innovation of our numerical investigations is the simulation of the three-dimensional non-steady secondary flows observed in the experiments. The flow with spiral vortices (regime S_1 described in §4.2) was obtained at $Re_2 = 0$ in the following way. The flow was sequentially calculated at several points (Re_1, Re_2), with the first point being at $Re_2 = 2050$ and the last one at $Re_2 = 0$. At each step the regime S_1 obtained at the preceding point was used as an initial condition. Numerical simulation performed with $Re_2 = 0$ and varying Re_1 has shown that the S_1 flow exists for $Re_1 > 1306 \pm (1)$. Decreasing Re_1 through this lower boundary of the existence region leads to a transition $S_1 \rightarrow$ I.

The angular velocity of regime S_1 is shown in figure 9 as a function of Re_1. One can see (in comparison with the wave speed calculated at $Re_2 = 2050$) that the velocity depends strongly on Re_2, rather than on Re_1.

Another comparison that can be made is between the wave speeds of the nonlinear secondary regime S_1 and of unstable travelling wave linear modes. As discussed above, an unstable basic flow solution (or regime II when $Re_1 > 1305$) can be calculated at $Re_1 > Re_{1c}$. When $1268.6 = Re_{1c} + 6.1 < Re_1 < 1332.2 = Re_{1c} + 69.8$, the solution is unstable not only to an axisymmetric anti-reflection-symmetric linear mode, but also

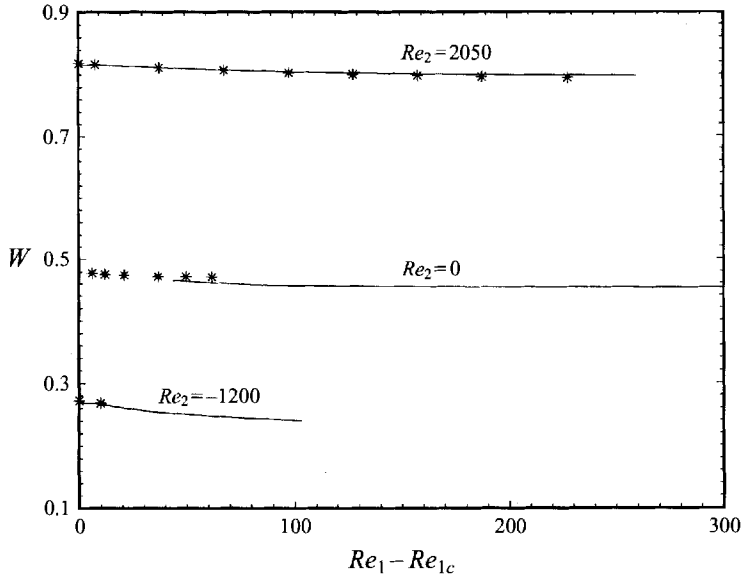

FIGURE 9. ——, Wave speed of secondary flows with spiral vortices (regime S_1 at $Re_2 = 0$ and 2050 and S_2 at $Re_2 = -1200$) as a function of $Re_1 - Re_{1c}$, where Re_{1c} is the critical number for the first instability of the basic flow, i.e. for transitions to regimes S_1, S_2 at $Re_2 = 2050$, -1200 and to regime I at $Re_2 = 0$; *, wave speed of the most unstable travelling wave linear mode at the same parameter values.

to an anti-reflection-symmetric mode $m = 1$. It can be seen in figure 9 that the wave speed of this mode matches closely the wave speed of regime S_1.

Another experimentally observed three-dimensional phenomenon is that increase of Re_1 gives rise to sinusoidal travelling waves on the Taylor vortices of regimes I and II. Our numerical investigation of these transitions was restricted to the linear stability analysis. Regimes I and II become unstable at $Re_1 = 1358.5$ and $Re_1 = 1497.1$ respectively. The preferred modes are travelling waves which are anti-reflection-symmetric and have wavenumbers $m = 3$ (for regime I) and $m = 5$ (for regime II). In both cases a further increase of Re_1 causes the steady flow to become unstable to a wide band of travelling wave linear modes, which includes anti-reflection-symmetric as well as reflection-symmetric ones. The waves propagate in the sense of rotation of the inner sphere. The wave speed of the most unstable mode at the stability limit is $W = 0.458$ for regime I and $W = 0.442$ for regime II. A comparison with the experimental results concerning the wavy Taylor-vortex flow between rotating spheres can be made. The critical Reynolds numbers are compared in Appendix B. Nakabayashi & Tsuchida (1988*b*) measured the wave speed in the flow with two pairs of wavy Taylor vortices at $\delta = 0.138$ and $Re_2 = 0$. They found that at the lower boundary of existence of this regime, $W = 0.48$ and $m = 5$.

4.2. *Co-rotating spheres; $Re_2 > 1811$*

The experiments by Yavorskaya *et al.* (1977, 1980), and Yavorskaya & Belyaev (1986) disclosed that at $Re_2 > 1940$ the first instability of the basic flow results in a travelling azimuthal wave flow with equatorially asymmetric spiral vortices located near the equator. Fast acceleration of the inner sphere from a subcritical value of Re_1 up to a slightly supercritical one was found to give rise to another transition to the flow with one pair of Taylor vortices. The existence regions of the flows with spiral and

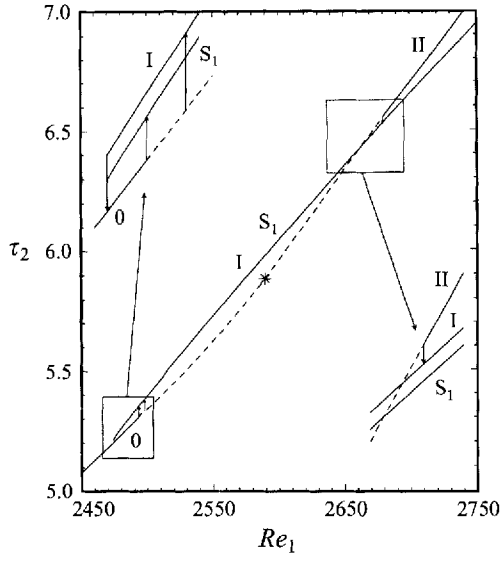

FIGURE 10. Bifurcation diagram at $Re_2 = 2050$ (plotted as in figure 7).

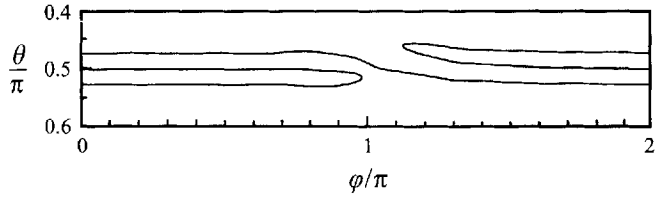

FIGURE 11. The flow with spiral vortices (regime S_1) at $Re_2 = 2050$, $Re_1 = 2513 = Re_{1c}(Re_2) + 20.1$. Vortex boundaries defined as curves $v = 0$ at the spherical section $r = 1 + 6\delta/11$. The section is mapped into a (φ, θ)-rectangle and only the part near the equator is plotted.

Taylor vortices overlap in large measure. The backwards transitions from either of these flows to the basic flow occur at the same (within the accuracy of measurements) subcritical value of Re_1. At higher Re_1 the non-uniqueness of secondary regimes is further enhanced by the appearance of the flow with two pairs of Taylor vortices near the equator. The transition from the basic flow to this secondary flow was produced in the experiments by fast acceleration of the inner sphere.

The bifurcation diagram constructed at $Re_2 = 2050$ and shown in figure 10 explains the laboratory observations.

When $Re_1 = Re_{1c} = 2492.9$, the basic flow becomes unstable to an $m = 4$ travelling wave mode, which is anti-reflection-symmetric. The primary bifurcation of the basic flow breaks the rotational and equatorial symmetry. The transition $0 \rightarrow S_1$ to the three-dimensional travelling wave secondary flow with spiral vortices was produced by starting with the basic flow equilibrium at $Re_1 = Re_{1c}$ and then suddenly increasing Re_1 to the value $Re_1 = 2495$ at which travelling wave anti-reflection-symmetric linear modes with $2 \leqslant m \leqslant 5$ are unstable. With the goal of reducing the computational time a finite perturbation consisting of a superposition of growing linear modes was added to the basic flow solution. The total energy of the initial perturbation was one-hundredth that of the basic flow.

The spatial structure of the computed secondary flow is shown in figures 11 and 12. Inflow and outflow curves (spiral vortex boundaries) are plotted in figure 11. More

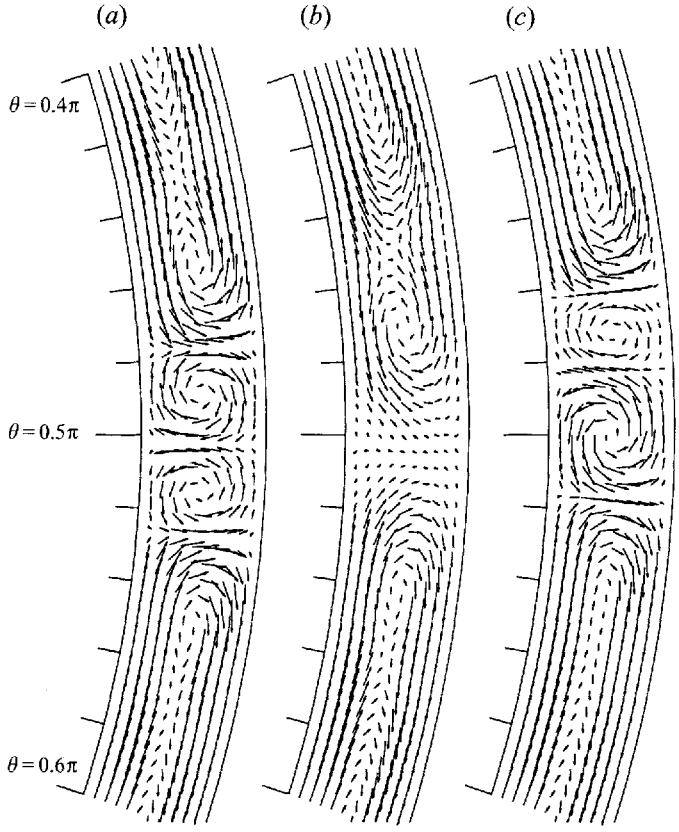

FIGURE 12. (r, θ)-projections of the velocity field of the flow in figure 11 plotted in the meridional sections crossed at $\varphi = 0.8\pi$, 0.95π, 1.2π $(a$–$c)$.

comprehensive information can be found in figure 12 where the meridional velocity fields in sections at different values of φ are shown. It can be seen that in a major range of the azimuthal angle the flow resembles the axisymmetric regime I (figure 12*a*). Two approximately equal vortices are located near the equator. The vortices have a meridional size that is slightly less than the gap width. A meridional circulation corresponding to the pinched basic flow is retained at higher and lower latitude. There is an inflow boundary between the vortices which lies near the equator and two outflow boundaries between the vortex pair and the regions of basic circulation. All the boundaries are almost straight streamlines extending from the inner to the outer sphere. A distinction between the regimes I and S_1 is due to the form of the spiral vortex flow near the point that is approximately $\varphi = \pi$ in figure 11. The vortices open up, their axes deviating toward the poles and their tails being eroded by the basic flow at higher and lower latitude. It is this part of the flow that is 'responsible' for the equatorial asymmetry of the flow (figure 12*c*). One can see in figures 11 and 12 (*b*) that there is a range of φ where the regions of basic circulation reach the equator, and the flow resembles the pinched basic flow with only one outflow boundary near the equator.

The whole pattern rotates in the direction of the inner-sphere rotation. The angular velocity W, which is plotted in figure 9, depends only slightly on Re_1. As discussed below, the basic flow solution can be calculated in the region $Re_1 > Re_{1c}$. A linear stability analysis reveals that at slightly supercritical Re_1 the basic flow becomes

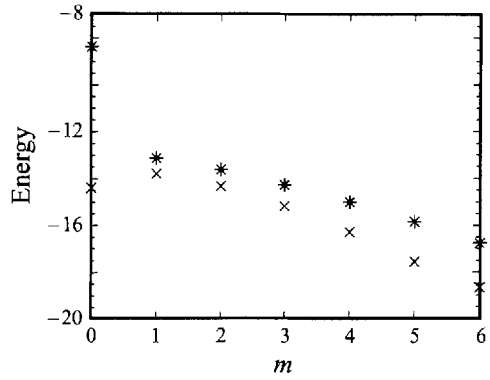

FIGURE 13. Azimuthal decomposition (2.17) of the total energy of reflection-symmetric ($\ln(E_m^s)$ denoted as *) and anti-reflection-symmetric ($\ln(E_m^a)$ denoted as $\times$) parts of the flow in figure 11. The energy corresponding to the Stokes term w^{St} is subtracted from E_0^s.

unstable to a wide band of travelling waves which have equal (to the third decimal place) wave speed. One can see in figure 9 that this wave speed is very nearly equal to that of the secondary nonlinear regime S_1.

We can state with assurance that the flow obtained is a numerical reproduction of the experimentally detected flow with spiral vortices. (A photograph from the experiments can be found in Yavorskaya *et al.* 1980; Yavorskaya & Belyaev 1986.) In particular, as in the experiments, the flow appears to have the main azimuthal wavenumber $m = 1$. This can also be seen in figure 13, where the distribution of the total energy of the flow over the reflection-symmetric and anti-reflection-symmetric components with different m is shown. On the other hand, the most unstable linear mode at the stability limit $Re_1 = Re_{1c}$ has $m = 4$. An explanation of this change of the azimuthal periodicity can be given which is based on the following results of the calculations. Firstly, many more linear modes become unstable at Reynolds numbers just higher than Re_{1c}. As an example, modes $m = 3, 5$, and 2 have zero growth rate at $Re_{1c} + 0.1$, $Re_{1c} + 1.1$, and $Re_{1c} + 1.4$, respectively. Therefore the transition $0 \rightarrow S_1$ simulated with $Re_{1c} + 2.1$ cannot be considered as produced under a quasi-static increase of Re_1. Secondly, as discussed below, the transition is subcritical. We may suppose that the azimuthal periodicity of regime S_1 points to the presence of several bifurcation points crossed by the solution on its way to the final equilibrium.

By imposing axial symmetry of the flow on our numerical code, the branch of basic flow solutions can be extended into the supercritical region $Re_1 > Re_{1c}$. At $Re_1 = 2497 = Re_{1c} + 4.1$, an axisymmetric, anti-reflection-symmetric linear mode is added to the set of unstable modes. When restricting ourselves to axisymmetric solutions and increasing Re_1 quasi-statically, we are in a position to obtain at this point the transition $0 \rightarrow$ I which is similar to that calculated with $Re_2 = 0$ and described in §4.1. One can see in figure 10 that regimes I and S_1 coexist over a wide range of Re_1, with the curve $\tau_2(Re_1)$ for regime I lying slightly higher than that for regime S_1. Curiously, it was found that starting from an unstable basic equilibrium at Re_1 belonging to the coexistence region of regimes I and S_1, our numerical code released from the axisymmetry constraint produces the transition $0 \rightarrow S_1$ only if a particular finite three-dimensional perturbation is added; otherwise the transition $0 \rightarrow$ I occurs.

Regimes I and S_1 can be obtained in the subcritical region $Re_1 < Re_{1c}$ by quasi-

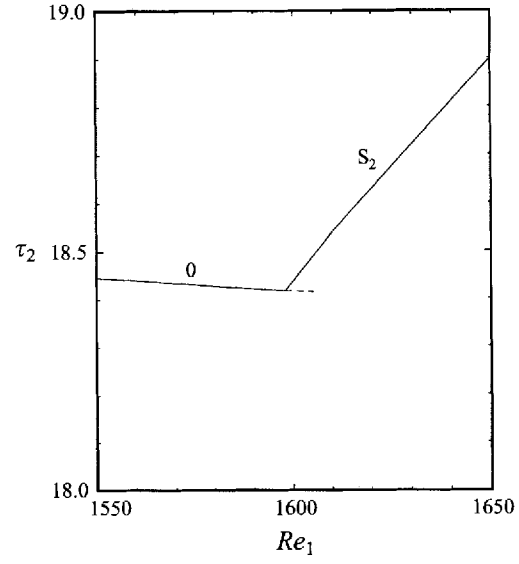

FIGURE 14. Bifurcation diagram at $Re_2 = -1200$ (plotted as in figure 7). S_2 denotes the flow with rotating spiral vortices shown in figures 15 and 16.

static decrease of Re_1. The backwards transitions $S_1 \rightarrow 0$ and $I \rightarrow 0$ occur at the close Reynolds numbers $Re_1 = 2473.8$ for $I \rightarrow 0$ and $2473 < Re_1 < 2474.5$ for $S_1 \rightarrow 0$.

An extension of the branch of basic equilibria to values of Re_1 higher than the critical value for transition $0 \rightarrow I$ is possible provided reflection symmetry of the flow is imposed. At $Re_1 = 2592 \pm (0.5)$, a smooth transformation of regime 0 to regime II occurs, which is similar to the transformation at $Re_2 = 0$ described above. At $Re_1 = 2681.1$, regime II becomes stable. The transition $II \rightarrow I$ is produced at this point by quasi-static decrease of Re_1.

During the calculations the branches of regimes I and II were extended up to $Re_1 = 2900$. The linear stability analysis has shown that the regimes are stable in this region. This does not preclude the existence of travelling wave instability of these regimes, which is similar to that detected at $Re_2 = 0$ (see §4.1) and corresponds to the appearance of sinusoidal waves on Taylor vortices, at greater values of Re_1. Unfortunately, there is no experimental information about the presence or absence of secondary regimes with wavy Taylor vortices at large positive Re_2.

4.3. *Counter-rotating spheres; $Re_2 < -646$*

Some experimental observations of the secondary regimes in this region are available. It was discovered by Yavorskaya *et al.* (1977, 80) and Yavorskaya & Belyaev (1986) that at $Re_2 < -920$ the first instability of the basic flow results in transition into the travelling wave flow with spiral vortices near the equator. The spirals differ in appearance from those of regime S_1.

The linear stability analysis of the basic flow revealed that at $Re_2 < -646$ the first instability is associated with reflection-symmetric travelling waves. Therefore, we can add a third type of primary symmetry-breaking bifurcation to the set of those described above. This bifurcation breaks the rotational symmetry and keeps the equatorial symmetry unbroken.

The nonlinear simulation was performed only with $Re_2 = -1200$. The resulting bifurcation diagram is shown in figure 14. At $Re_1 = 1597.3$ the basic flow becomes

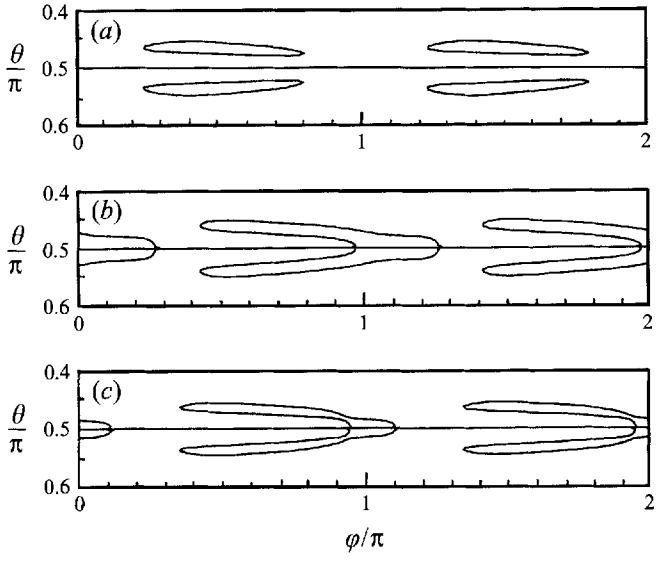

FIGURE 15. The flow with spiral vortices (regime S_2) at $Re_2 = -1200, Re_1 = 1630 = Re_{1c}(Re_2) + 32.7$. Vortex boundaries (plotted as in figure 11) at the sections $r = 1 + \delta/4,\ 1 + \delta/2,\ 1 + 3\delta/4$ (a–c)

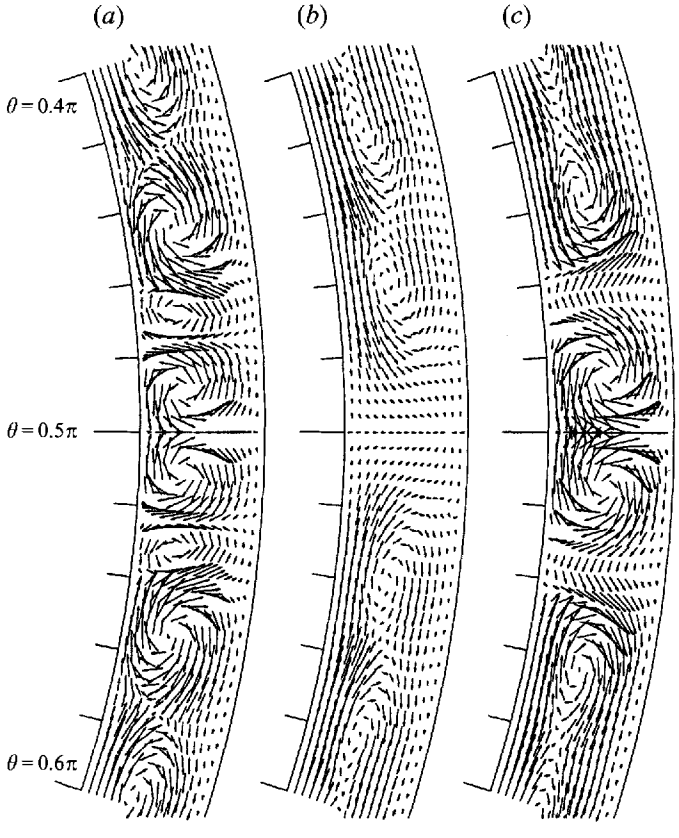

FIGURE 16. (r, θ)-projections of the velocity field of the flow in figure 15 at $\varphi = 0.7\pi,\ \pi,\ 1.3\pi$ (a–c)

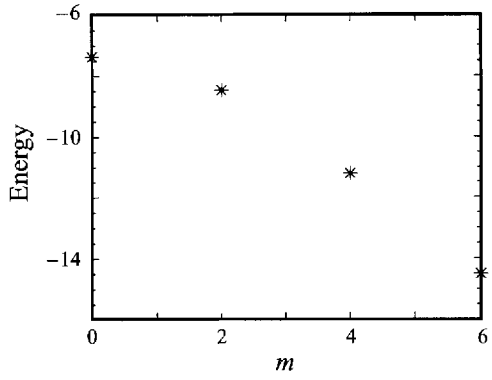

FIGURE 17. Azimuthal decomposition of the total energy of the flow in figure 15. Only reflection-symmetric terms with even m ($\ln(E_m^s)$ denoted as *) are non-zero.

unstable to a linear mode with wavenumber $m = 2$. The transition to a spiral vortex flow can be produced at the stability limit in a way which is similar to that described in §4.2 for the transition $0 \rightarrow S_1$, that is, by suddenly increasing Re_1 to the supercritical value $Re_1 = 1601$ and adding a three-dimensional finite perturbation. The perturbation is the superposition of the preferred mode $m = 2$ and the reflection-symmetric travelling wave mode $m = 1$ which becomes unstable at $Re_1 = 1599.4$.

Hereafter the resulting flow will be referred to as regime S_2. Its spatial structure is shown in figures 15 and 16. It can be seen that, unlike regime S_1, vortices do not fill the whole gap width (compare figure 16 with 12). There is a clearance between them and the outer sphere. The flow pattern depends strongly on r. Furthermore, there are ranges of φ in which the flow resembles the axisymmetric regime II, that is, two vortices with an outflow boundary between them are located at the equator and are separated from the basic meridional flow by smaller vortices having the opposite sign of circulation (figure 16*a*).

Other distinctions between regimes S_2 and S_1 are that regime S_2 has the main azimuthal wavenumber $m = 2$ and is reflection-symmetric. The decomposition of the flow energy is shown in figure 17. It can be seen that in accordance with the type of equatorial symmetry and the azimuthal periodicity of the linear mode which first becomes unstable only the reflection-symmetric terms with even wavenumber are non-zero.

The wave-speed of regime S_2, which is depicted in figure 9, is substantially less than that of regime S_1 at $Re_2 = 0$ or $Re_2 = 2050$. The results of the linear stability analysis, namely the wave speeds of the preferred mode $m = 2$ at $Re_2 = -1200$, are also shown in figure 9. One can see that the speeds of nonlinear and linear solutions are very close. This is not the case when the other unstable mode $m = 1$ is taken for comparison. The wave speed of this mode, which is about 0.19, differs significantly from those of regime S_2 and mode $m = 2$.

An essential property of the instability is that the bifurcation appears to be supercritical. The Reynolds number for transition $0 \rightarrow S_2$ was defined by the linear stability analysis as $Re_1 = 1597.3$. The maximum value of Re_1 at which the backwards transition $S_2 \rightarrow 0$ was produced by our nonlinear code is $Re_1 = 1597$.

An unstable basic flow solution can be extended into the supercritical region by imposing axisymmetry. With this constraint, the flow breaks into axisymmetric oscillations at $Re_1 = 1609 \pm (2)$. The oscillations change the spatial structure of the flow from that of the basic flow to that of regime II and back during the period, with

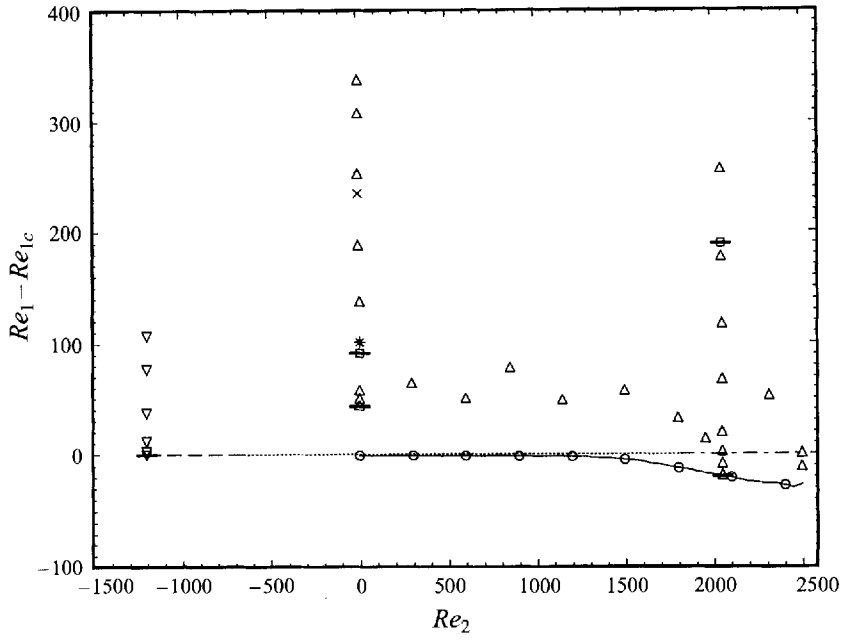

FIGURE 18. Summary plot of the calculated secondary regimes of the flow. $Re_1 - Re_{1c}$ is plotted on the vertical axis instead of Re_1, where $Re_{1c}(Re_2)$ is the critical number for the first instability of the basic flow determined by the linear stability analysis. Therefore, the zero-ordinate line corresponds to the stability curve and separates subcritical and supercritical regions. — — — —, ·····, — · — · —, three different parts of the linear stability curve corresponding to the three different types of primary bifurcation; △ and —△—, points at which spiral vortex regime S_1 was calculated and the lower boundary of its existence region at $Re_2 = 0$, 2050; ▽ and —▽—, points at $Re_2 = -1200$ at which spiral vortex regime S_2 was calculated and the lower boundary of its existence region; —○—○—○—, the lower boundary of existence region of regime I; —□—, the lower boundary of existence region of regime II calculated at $Re_2 = 0$, 2050; * and ×, limits of the wave instability of regimes I and II calculated at $Re_2 = 0$.

reflection and rotational symmetries remaining unchanged. This flow is unstable to three-dimensional disturbances and undergoes a transition to regime S_2 after being released from the artificial condition of axisymmetry. It is to be noted that a similar axisymmetric oscillating flow was found to be stable in wider layers (see Astaf'eva 1985*a* for the case $\delta = 0.24$).

5. Concluding remarks

In this paper we have investigated the various regimes of spherical Couette flow and transitions among them. The case of a small gap size and both boundary spheres rotating has been considered. Four secondary flows were involved in the calculations: the steady axisymmetric flows with one and two pairs of Taylor vortices and two different three-dimensional flows with rotating spiral vortices near the equator. This study is believed to be the first to simulate the spiral vortex flows arising in thin layers when both boundary spheres rotate. The numerical results provide a detailed description of observed three-dimensional flows and the pattern of transitions among various regimes. They also explain many of the experimental observations, among them that some transitions occur only when the inner sphere is accelerated or decelerated quickly, whereas others occur when the acceleration or deceleration is

slow. One can see in the calculated bifurcation diagrams displayed in figures 7, 10, and 14 that the transitions which can be assigned to the first group are $0 \rightarrow$ II, II$\rightarrow 0$, $0 \rightarrow$ I at $Re_2 = 2050$ and $0 \rightarrow$ II, II $\rightarrow 0$ at $Re_2 = 0$, and the transitions belonging to the second group are $0 \rightarrow S_1$, $S_1 \rightarrow 0$, I $\rightarrow 0$, II $\rightarrow$ I at $Re_2 = 2050$, $0 \rightarrow$ I, I $\rightarrow 0$, $S_1 \rightarrow$ I, II $\rightarrow$ I at $Re_2 = 0$ and $0 \rightarrow S_2$, $S_2 \rightarrow 0$ at $Re_2 = -1200$.

The results of the calculations are summarized in figure 18. It can be seen that the study can be continued, in particular, to obtain the complete boundaries of the existence regions of the secondary regimes S_1, S_2, I, and II. Another possible subject to investigate is the influence of the gap size δ on the bifurcations.

The principal conclusion which can be drawn from the results presented in this paper is the following. The parameter range under consideration ($\delta = 0.11, -1200 \leqslant Re_2 \leqslant 2500$) can be divided into three parts depending on the type of primary symmetry-breaking bifurcation. At $-646 < Re_2 < 1811$ the bifurcation is a subcritical pitchfork breaking equatorial symmetry, leading to an equatorially asymmetric transition to the steady axisymmetric but also reflection-symmetric flow with one pair of Taylor vortices. At $Re_2 < -646$ and $Re_2 > 1811$ the bifurcation breaks the rotational symmetry and causes azimuthally travelling wave secondary flows with spiral vortices to appear at the stability limit. The difference between the last two regions is that in the first the equatorial symmetry is preserved and the travelling wave solution branches off supercritically, whereas in the second the bifurcation is subcritical and breaks not only rotational but also equatorial symmetry, resulting in an equatorially asymmetric secondary solution.

We believe that the semi-spectral numerical technique employed here has demonstrated its capability for reproduction of the three-dimensional flows of viscous incompressible fluid in a spherical annulus. Up to now, there has been only one study carried out by Dumas (1994) that investigated numerically the experimentally detected phenomenon of three-dimensional instability in thick layers with $\delta \geqslant 0.33$. It seems plausible that these interesting investigations can be pursued with the use of the technique outlined above. It is also possible that our numerical method can be applied to the fascinating problem of convection in a spherical layer.

The investigations were began on the initiative of I. M. Yavorskaya. Her help cannot be overestimated. The author thanks N. M. Astaf'eva, Yu. N. Belyaev and N. D. Vvedenskaya for many useful discussions. He is very grateful to the referees for careful reviews of the paper and constructive comments. This work was supported in parts by the Russian Fund for fundamental research (grants 93-013-2896 and 93-013-17342), the International Science Foundation (grant J2P100), and the Alexander von Humboldt Foundation.

Appendix A

We demonstrate below that the nonlinear right-hand sides of (2.10) can be given in terms of the following products of spherical harmonics:

$$G_a = Y_{l_1}^{m_1} Y_{l_2}^{m_2}, \tag{A 1}$$

$$G_b = (\sin\theta)^{-1} \left(\frac{\partial Y_{l_1}^{m_1}}{\partial \theta} \frac{\partial Y_{l_2}^{m_2}}{\partial \varphi} - \frac{\partial Y_{l_1}^{m_1}}{\partial \varphi} \frac{\partial Y_{l_2}^{m_2}}{\partial \theta} \right), \tag{A 2}$$

$$G_c = (\sin\theta)^{-2} \frac{\partial Y_{l_1}^{m_1}}{\partial \varphi} \frac{\partial Y_{l_2}^{m_2}}{\partial \varphi} + \frac{\partial Y_{l_1}^{m_1}}{\partial \theta} \frac{\partial Y_{l_2}^{m_2}}{\partial \theta}. \tag{A 3}$$

Sums of a similar nature were written by Young (1974) for the equations describing thermal convection in a spherical shell. Each of (A1)–(A3) can be expanded in a finite series of spherical harmonics and, thus, the right-hand sides of (2.10) are expandable in a like manner. For brevity, the subscript i ($i = 1, 2$) will identify the coefficient with the subscripts l_i, m_i. For example, T_1 will denote $T_{l_1 m_1}$. In addition, we shall use the following designations: $b_i = l_i(l_i + 1)$, $D_i = D_{l_i} = l_i(l_i + 1)r^{-2} - \partial^2/\partial r^2$. We obtain

$$\Phi^T = \frac{1}{\sin\theta}\left(\frac{\partial F^v}{\partial \varphi} - \frac{\partial}{\partial \theta}(\sin\theta F^w)\right) = \sum_{m_1,l_1}\sum_{m_2,l_2} r^{-3}\left[b_1 b_2\left(Q_1 T_2 - S_1\frac{\partial T_2}{\partial r}\right)G_a\right.$$
$$\left. + (b_2 T_1 T_2 + b_1 S_1 D_2(S_2))G_b + \left(b_1 S_1\frac{\partial T_2}{\partial r} - b_2 Q_1 T_2\right)G_c\right],$$

$$\Phi^S = -F^u = \sum_{m_1,l_1}\sum_{m_2,l_2} r^{-3}[-r^{-1}b_1 b_2 S_1 S_2 G_a + (r^{-1}b_2 T_1 S_2 - T_1 Q_2 + Q_1 T_2)G_b$$
$$+ (-r^{-1}b_2 Q_1 S_2 + T_1 T_2 + Q_1 Q_2)G_c],$$

$$\Phi^Q = \frac{1}{\sin\theta}\left(\frac{\partial F^w}{\partial \varphi} + \frac{\partial}{\partial \theta}(\sin\theta F^v)\right) = \sum_{m_1,l_1}\sum_{m_2,l_2} r^{-3}\left\{b_1 b_2(S_1 D_2(S_2) - T_1 T_2)G_a\right.$$
$$+ \left(b_1 S_1\frac{\partial T_2}{\partial r} + b_2 Q_1 T_2\right)G_b + (-b_1 S_1 D_2(S_2) + b_2 T_1 T_2)G_c$$
$$\left. -\tfrac{1}{2}L^2[r^{-2}b_1 b_2 S_1 S_2 G_a + (Q_1 T_2 - T_1 Q_2)G_b + (T_1 T_2 + Q_1 Q_2)G_c]\right\},$$

where L^2 is the θ–φ part of the Laplacian

$$L^2 = -(\sin\theta)^{-1}\frac{\partial}{\partial\theta}\sin\theta\frac{\partial}{\partial\theta} - (\sin\theta)^{-2}\frac{\partial^2}{\partial\varphi^2}, \qquad L^2 Y_l^m = l(l+1)Y_l^m.$$

Appendix B

The intention of this section is to check our calculations for accuracy by comparing the results with the known experimental data. Also discussed is the effect of values of discretization parameters K, M, L, and time step Δt on the accuracy. Out of the extensive experimental results obtained by the group of Yavorskaya and Belyaev (Yavorskaya *et al.* 1977, 1980; Yavorskaya & Belyaev 1986) for the layer with gap size $\delta = 0.1096$ we choose for comparison those for the specific case of fixed outer sphere ($Re_2 = 0$), since the transitions among secondary regimes have been well understood and documented in this case. For the most part, the experimental results are represented graphically in the papers. The exact values of Taylor vortex sizes and critical Reynolds numbers for transitions, which are used below, were communicated privately by Yu. N. Belyaev (1994).

The major portion of our numerical simulation was performed with the following discretization parameters: $K = 10$, $M = 6$ (0 when calculating axisymmetric flows), and $L = 60$, where K, M, and L are respectively the number of radial discretization points and test functions in the azimuthal and polar directions. In the region of large negative Re_2, intense counter-rotation of the boundary spheres results in a strong radial gradient of the velocity field. Therefore, it was necessary at $Re_2 < -646$ to raise the radial discretization parameter K up to 15. The control calculations of axisymmetric flows carried out with $K = 15, 20, 25$ at $Re_2 = 0$ and 2050 and with

K	10	15	20	25
$0 \rightarrow \mathrm{I}$	1262.5	1255.1	1254.9	1254.9
$\mathrm{I} \rightarrow 0$	1261.2	1253.9	1253.8	1253.8

TABLE 1. The influence of K (the number of radial discretization points) on the critical numbers for transitions $0 \rightarrow \mathrm{I}$ and $\mathrm{I} \rightarrow 0$. Calculations are carried out with $Re_2 = 0$ and $L = 60$.

$K = 20$, 25 at $Re_2 = -1200$ produced results (the sequence of transitions, the critical Reynolds numbers for them, torques on the boundary spheres, etc.) which differ little from those with $K = 10$ and $K = 15$. An example of such a test can be seen in Table 1, where the critical Reynolds numbers for transitions $0 \rightarrow \mathrm{I}$ and $\mathrm{I} \rightarrow 0$ are compared. The calculations are made with $L = 60$.

The accuracy of our simulation of the three-dimensional flows was not tested by calculations with azimuthal truncation parameter M greater than 6. This can be justified to some extent by the good accord between calculations and experiments in the spatial structure of three-dimensional regimes and in the regions of their existence.

It must be stressed that the number L of Legendre functions in the expansions of unknown functions has a dramatic effect on the accuracy. Calculations with poor polar resolution give a wrong sequence of bifurcations and miss the secondary regimes detected in the experiments. For example, when using the numerical code with $L = 20$, $K = 10$, and $M = 0$ at $Re_2 = 0$, we were in a position to extend the branch of a basic equilibrium without any transition up to $Re_1 = 1500$, that is, into the supercritical region where the axisymmetric secondary regimes with one and two pairs of Taylor vortices exist. A simple qualitative analysis can be made. The characteristic polar scale of secondary flows with Taylor and spiral vortices and of a basic flow with pinches (the latitudinal extent of a Taylor or spiral vortex or a pinch) is slightly less than the gap width. Setting the angular size of a vortex at $\Delta\theta = 0.8\delta$ (see figure 19), the number of associated Legendre polynomial $l = \pi/\Delta\theta \approx 36$. It is evident that a simulation with this or smaller values of L cannot be plausible. Our calculations with different values of L have shown that $L = 60$ is the minimum value that provides valid results. The comparison of these results as well as of the results obtained with $L = 90$ with experimental data can be seen in table 2 and figure 19. The control calculations for axisymmetric regimes with $L = 110$ are not involved as they provide practically the same results as the calculations with $L = 90$.

The critical Reynolds numbers for transitions among different regimes and the size of Taylor vortices in regime I are chosen to compare our results with experimental ones. All measurements are made at $Re_2 = 0$. The critical Reynolds numbers for the transitions are shown in table 2. Six types of transitions are included: (i) the transition from the basic flow to the flow with one pair of Taylor vortices denoted as $0 \rightarrow \mathrm{I}$, (ii) the reverse transition $\mathrm{I} \rightarrow 0$, (iii, iv) the transitions $\mathrm{S_I} \rightarrow \mathrm{I}$ and $\mathrm{II} \rightarrow \mathrm{I}$, which correspond to the lower boundaries of existence regions of regimes $\mathrm{S_I}$ and II, (v, vi) the transitions from regimes I and II to the flows with wavy vortices (these are determined numerically by the linear stability analysis).

There is good agreement (within 5%) between the calculated and experimentally detected critical Reynolds numbers. It is to be noted that the Reynolds numbers were measured in the experiments accurate to ± 12.

One can see that our critical Reynolds numbers are about 4% higher than the experimental ones. The reason for such a regular discrepancy is unlikely to be the difference in gap size between the experiments ($\delta = 0.1096$) and calculations

Transition	Experiments		Calculations with $L = 60$		Calculations with $L = 90$	
	Re_1	ΔRe_1	Re_1	ΔRe_1	Re_1	ΔRe_1
$0 \rightarrow$ I	1225		1262.5		1262.2	
I $\rightarrow 0$	1225		1261.2	−1.3	1261.1	−1.1
$S_1 \rightarrow$ I	1270	45	1306.0	43.5		
II $\rightarrow$ I	1315	90	1365.2	102.7	1354.9	92.7
Wave instability of regime I	1300	75	1358.9	96.4	1358.5	96.3
Wave instability of regime II	1430	205	1489.5	227.0	1495.2	233.0

TABLE 2. The influence of L (the number of test functions in the polar direction) on the critical numbers for transitions among different regimes at $Re_2 = 0$. $\Delta Re_1 = Re_1 - Re_{1c}$, where Re_{1c} is the critical number (obtained in the experiments or calculated with $L = 60$ or $L = 90$) for the first instability of the basic flow, that is, for transition $0 \rightarrow$ I.

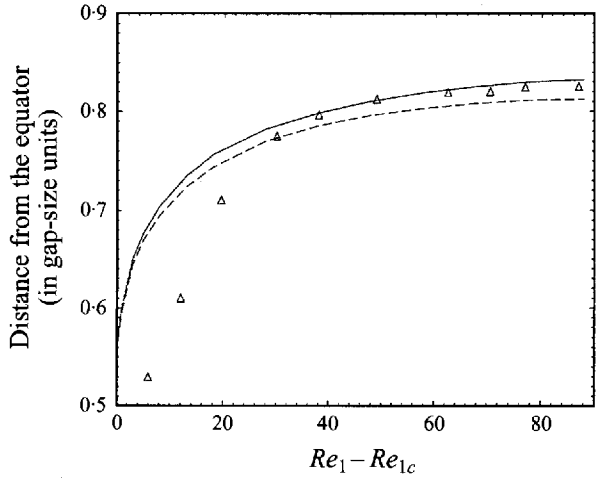

FIGURE 19. Size of vortex in regime I at $Re_2 = 0$ as a function of $Re_1 - Re_{1c}$. —— (– – – –), calculations with $L = 90$ ($L = 60$); △, experimental data. The value of Re_{1c} is 1262.2 (1262.5) for calculations with $L = 90$ ($L = 60$) and 1225 for the experiments.

($\delta = 0.11$). It was shown by Yavorskaya *et al.* (1980) that in the case of a thin layer, the critical Reynolds number for transition $0 \rightarrow$ I at $Re_1 = 0$ can be approximately defined as a function of δ by the formula $Re_{1c}(\delta) = 41.3(1 + c\delta)\delta^{-3/2}$, where $c \approx 1$. Setting $c = 1$, we obtain $Re_{1c}(0.1096) = 1263$ and $Re_{1c}(0.11) = 1257$, i.e. the discrepancy is considerably below than that shown in table 2 and has the opposite sign. A more probable reason is the inevitable geometric imperfection of the experimental spherical gap. As was shown numerically by Bar-Yoseph *et al.* (1990), the presence of a small eccentricity slightly decreases Re_{1c}. Furthermore, a misalignment of the axes of inner and outer boundary spheres may introduce a systematic error into the experimental measurement of the Reynolds number. In attempt to eliminate this unknown reason we compare the differences $Re_1 - Re_{1c}$, where Re_{1c} are the corresponding (experimental or calculated with $L = 60$ or $L = 90$) critical numbers for the first instability of the basic flow, i.e. for the transition $0 \rightarrow$ I. It can be seen

Δt	Eigenvalue at $Re_1 = 2512$	Re_{1c}	Wave speed at $Re_1 = Re_{1c}$
$\pi/50$	$-5.32 \times 10^{-3} - i3.277$	2518.2	0.819
$\pi/100$	$-4.14 \times 10^{-3} - i3.280$	2516.5	0.820
$\pi/200$	$-3.97 \times 10^{-3} - i3.280$	2516.4	0.820
$\pi/400$	$-3.95 \times 10^{-3} - i3.280$	2516.4	0.820

TABLE 3. The influence of time step Δt on the solution of linear stability problem. The stability of the basic flow to the preferred mode $m = 4$ is calculated with $Re_2 = 2075$, $L = 60$, $K = 10$.

in table 2 that the agreement between these differences is better than between the critical Reynolds numbers themselves.

The numerically and experimentally detected sizes of Taylor vortices in regime I are shown in figure 19 as functions of $Re_1 - Re_{1c}$. The case of a fixed outer sphere is considered. The vortex size is defined as the distance between the equator and the outflow boundary of the vortex. To facilitate comparison with visual experimental observations (necessarily made from the exterior), this outflow location is determined at the radial discretization point nearest to (but not at) the outer sphere.

The last numerical parameter whose influence on the accuracy should be discussed is the time step Δt. Test calculations with $\Delta t = \pi/50$, $\pi/100$, $\pi/200$, and $\pi/400$ have shown that the maximum value $\Delta t = \pi/50$ can be used for the nonlinear simulation. A decrease of Δt causes a slight change of the time of transition between two regimes, with the consequence of transitional states and a final state remaining unchanged. The influence of Δt on the solution of the linear stability problem is illustrated in table 3 by the example of anti-reflection-symmetric mode $m = 4$. It can be seen that the calculations with $\Delta t = \pi/50$ give an error in the eigenvalue and thus in the critical Reynolds number and wave speed. Therefore, the linear stability problem was solved with $\Delta t = \pi/100$ and, in specific cases, with $\Delta t = \pi/200$.

REFERENCES

ANDERECK, C. D., LIU, S. S. & SWINNEY, H. L. 1986 Flow regimes in a circular Couette system with independently rotating cylinders. *J. Fluid Mech.* **164**, 155–183.

ASTAF'EVA, N. M. 1985*a* Numerical simulation of spherical Couette flow asymmetric with respect to the equator. *Fluid Dyn.* **20**, *N*3, 383–387. (Transl. from *Izv. AN SSSR, Mekh. Zhid. i Gaza* 1985, *N*3, 56–62.)

ASTAF'EVA, N. M. 1985*b* Numerical solution of the problem on linear stability of the spherical Couette flow (in Russian). *Preprint* 1027. Space Research Institute, USSR Academy of Science, Moscow.

ASTAF'EVA, N. M., VVEDENSKAYA, N. D. & YAVORSKAYA, I. M. 1978 Numerical study of nonlinear axisymmetric flow of fluid between two concentric rotating spheres. In *Sixth Intl Conf. on Numerical Methods in Fluid Dynamics* (ed. H. Cabannes, M. Holt & V. Rusanov). Lecture Notes in Physics, vol. 90, pp. 56–63. Springer.

BAR-YOSEPH, P., SOLAN, A., HILEN, R. & ROESNER, K. G. 1990 Taylor vortex flow between eccentric coaxial rotating spheres. *Phys. Fluids* A **2**, 1564–1573.

BARTELS, F. 1982 Taylor vortices between two concentric rotating spheres. *J. Fluid Mech.* **119**, 1–25.

BELYAEV, YU. N., MONAKHOV, A. A., KHLEBUTIN, G. N. & YAVORSKAYA, I. M. 1980 Study of stability and nonuniqueness of secondary flows in rotating spherical layers (in Russian). *Preprint* 567. Space Research Institute, USSR Academy of Science, Moscow.

BELYAEV, YU. N., MONAKHOV, A. A. & YAVORSKAYA, I. M. 1978 Stability of spherical Couette flow in thick layers when the inner sphere revolves. *Fluid Dyn.* **13**, *N*2, 162–168. (Transl. from *Izv. AN SSSR, Mekh. Zhid. i Gaza* 1978, *N*2, 9–15.)

BONNET, J.-P. & ALZIARY DE ROQUEFORT, T. 1976 Ecoulement entre deux sphères concentriques en rotation. *J. Méc.* **15**, 373–397.

BÜHLER, K. 1990 Symmetric and asymmetric Taylor vortex flow in spherical gaps. *Acta Mechanica* **81**, 3–38.

BÜHLER, K. & ZIEREP, J. 1984 New secondary flow instabilities for high *Re*-number flow between two rotating spheres. In *Laminar-Turbulent Transition* (ed. V. V. Kozlov), pp. 677–685. Springer.

CHANDRASEKHAR, S. 1961 *Hydrodynamic and Hydromagnetic Stability*. Clarendon.

COLES, D. 1965 Transition in circular Couette flow. *J. Fluid Mech.* **21**, 385–425.

DUMAS, G. 1994 The spherical Couette flow and its large-gap stability by spectral simulation. In *CFD94*, CFD Society of Canada, Toronto.

DUMAS, G. & LEONARD, A. 1994 A divergence-free expansions spectral method for three-dimensional flows in spherical-gap geometries. *J. Comput. Phys.* **111**, 205–219.

GODUNOV, S. K. & RYABENKI, V. S. 1964 *Theory of Differerence Schemes*. North-Holland.

JOSEPH, D. D. 1976 *Stability of Fluid Motion* I. Springer.

KHLEBUTIN, G. N. 1968 Stability of fluid motion between a rotating and a stationary concentric sphere. *Fluid Dyn.* **3**, *N*6, 31–32. (Transl. from *Izv. AN SSSR. Mekh. Zhid. i Gaza* 1968, *N*6, 53–56.)

KOTSCHIN, N. E., KIBEL, I. A. & ROSE, N. V. 1955 *Theoretische Hydromechanik* II. Akademie, Berlin.

KRUEGER, E. R., GROSS, A. & DIPRIMA, R. C. 1966 On the relative importance of Taylor-vortex and non-axisymmetric modes in flow between rotating cylinders. *J. Fluid Mech.* **24**, 521–538.

LANGFORD, W. F., TAGG, R., KOSTELICH, E. J., SWINNEY, H. L. & GOLUBITSKY, M. 1988 Primary instabilities and bifurcality in flow between counter-rotating cylinders. *Phys. Fluids* **31**, 776–785.

MAMUN, C. K. & TUCKERMAN, L. S. 1995 Asymmetry and Hopf bifurcation in spherical Couette flow. *Phys. Fluids* **7**, 80–91.

MARCUS, P. S. & TUCKERMAN, L. S. 1987 Simulation of flow between concentric rotating spheres. *J. Fluid Mech.* **185**, 1–65.

MUNSON, B. R. & JOSEPH, D. D. 1971 Viscous incompressible flow between concentric rotating spheres. Part 1. Basic flow. *J. Fluid Mech.* **49**, 289–303.

NAKABAYASHI, K. 1983 Transition of Taylor–Görtler vortex flow in spherical Couette flow. *J. Fluid Mech.* **132**, 209–230.

NAKABAYASHI, K. & TSUCHIDA, YO. 1988*a* Spectral study of the laminar-turbulent transition in spherical Couette flow. *J. Fluid Mech.* **194**, 101–132.

NAKABAYASHI, K. & TSUCHIDA, YO. 1988*b* Modulated and unmodulated travelling azimuthal waves on the toroidal vortices in a spherical Couette system. *J. Fluid Mech.* **195**, 495–522.

ORSZAG, S. A. 1974 Fourier series on spheres. *Mon. Weather Rev.* **102**, 56–75.

OVSEENKO, YU. G. 1963 On the motion of a viscous liquid between two rotating spheres (in Russian). *Izv. Vyssh. Ucheb. Zaved. Mat. N*4, 129–139.

RUELLE, D. 1973 Bifurcations in the presence of a symmetry group. *Arch. Rat. Mech. Anal.* **51**, 136–152.

SCHRAUF, G. 1986 The first instability in spherical Taylor–Couette flow. *J. Fluid Mech.* **166**, 287–303.

WIMMER, M. 1976 Experiments on a viscious fluid flow between concentric rotating spheres. *J. Fluid Mech.* **78**, 317–335.

WIMMER, M. 1977 Experimentelle Untersuchung der Strömung zwischen konzentrischen, rotierenden Kugeln. *Z. Angew. Math. Mech.* **57**, 218–219.

WIMMER, M. 1981 Experiments on the stability of viscous flow between two concentric rotating spheres. *J. Fluid Mech.* **103**, 117–131.

YAVORSKAYA, I. M. & BELYAEV, YU. N. 1986 Hydrodynamic stability in rotating spherical layers: application to dynamics of planetary atmospheres. *Acta Astrounautica* **13**, *N*6/7, 433–440.

YAVORSKAYA, I. M., BELYAEV, YU. N. & MONAKHOV, A. A. 1977 Stability investigations and secondary flows in rotating spherical layers at arbitrary Rossby number. *Sov. Phys. Dokl.* **22**, 717–719. (Transl. from *Dokl. Akad. Nauk SSSR*, 1977, **237**, 804–807.)

YAVORSKAYA, I. M., BELYAEV, YU. N., MONAKHOV, A. A., ASTAF'EVA, N. M., SCHERBAKOV, S. A. & VVEDENSKAYA, N. D. 1980 Stability, non-uniqueness and transition to turbulence in the flow between two rotating spheres. In *Theoretical and Applied Mechanics* (ed. F. P. J. Rimrott & B. Tabarrok), pp. 431–443. North-Holland.

YAVORSKAYA, I. M., VVEDENSKAYA, N. D. & ASTAF'EVA, N. M. 1978 On stability and nonuniqueness of fluid flows in rotating spherical layers. *Dokl. Akad. Nauk SSSR* **241**, 52–55.

YOUNG, R. E. 1974 Finite-amplitude thermal convection in a spherical shell. *J. Fluid Mech.* **63**, 695–721.

ZIKANOV, O. YU. 1993*a* Numerical study of instability of viscous fluid flows in rotating volumes (in Russian). Kand. of Sci. thesis, Moscow State University, Moscow.

ZIKANOV, O. YU. 1993*b* Numerical simulation of the first instability in spherical Couette flow. *Preprint* 531. Institute for Problems in Mechanics, Russian Academy of Science, Moscow.

ZIKANOV, O. YU. 1995 Numerical simulation of instability and secondary regimes in spherical Couette flow (in Russian). *Izv. AN SSSR, Mech. Zhid. i Gaza N*1, 1–15.